Numerical simulations of seismicity-induced fluid flow in the Tjornes Fracture Zone, Iceland

Numerical simulations of seismicity-induced fluid flow in the Tjörnes Fracture Zone, Iceland

M. Lupi,[1] S. Geiger,[2] and C. M. Graham[3]

Received 27 May 2010; revised 22 March 2011; accepted 7 April 2011; published 7 July 2011.

[1] We use high-resolution simulations to analyze fluid flow, pore pressure, and fault permeability evolution in the seismically active Tjörnes Fracture Zone (TFZ), a major transform fault zone in the North of Iceland. Our results show that the TFZ is characterized by four distinct areas where pore pressures are above hydrostatic, consistent with geophysical observations. Basement and faults, which are assumed to have low permeabilities, often display pore pressures close to lithostatic. Fault permeabilities are allowed to vary freely as a function of the effective fault normal stress. They hence inflate periodically to release excess pore pressure in a few minutes. This is accompanied by an increase in permeability of over seven orders of magnitude and causes short-lived fluid fluxes of more than 0.01 m s^{-1}. After pore pressures have dissipated, fault permeabilities decay back to their original values in 2 to 3 years as the effective fault normal stress increases. This behavior is consistent with a toggle switch mechanism and could have two important implications for fluid flow in seismically and hydrothermally active oceanic crust. First, the rapid changes in fault permeability and pore pressure provide an explanation for distinct cyclical geochemical changes observed on a similar timescale in thermal waters near the town of Húsavik in the TFZ before and after a magnitude 5.8 M_w earthquake. Second, our results provide another line of evidence in the growing number of observations that crustal permeabilities are constantly evolving and geological processes in hydrothermal systems can be dominated by short-lived and extreme flow events.

Citation: Lupi, M., S. Geiger, and C. M. Graham (2011), Numerical simulations of seismicity-induced fluid flow in the Tjörnes Fracture Zone, Iceland, *J. Geophys. Res.*, *116*, B07101, doi:10.1029/2010JB007732.

1. Introduction

[2] Iceland has formed by the interaction of the Mid Atlantic Ridge and the Icelandic hot spot plume [*Darbyshire et al.*, 1998; *Allen et al.*, 2002; *Bjarnason*, 2008]. The resulting scenario is a geodynamically active and geologically young system. The oldest rocks, of Tertiary age, crop out in NW and E Iceland while the central areas that bound the Mid Atlantic Ridge are characterized by Quaternary to recent lithologies. Iceland has been one of the most studied natural laboratories due to its strong volcanism, active tectonics, and intense seismicity. The Mid Atlantic Ridge runs across Iceland and is clearly recognizable in the geology of the central region, which consists of elongated ridge fissures and faulted areas. In the South and North of Iceland, the Mid Atlantic Ridge is offset by two transform areas: the South Iceland Seismic Zone (SISZ) and the Tjörnes Fracture Zone (TFZ). These regions are affected by intense seismicity [*Stefánsson et al.*, 2003, 2008], which is continuously monitored by the South Iceland Lowland automatic network [*Bodvarsson et al.*, 1996; *Jakobsdóttir*, 2008].

[3] The TFZ (Figure 1) in northern Iceland is an offshore rift-ridge transform zone [*Gudmundsson*, 2007] consisting of faulted sedimentary basins and crystalline basement [*Riedel et al.*, 2005]. Two types of seismic events occur in the TFZ: high-magnitude (magnitude larger than 5 M_w) earthquakes due to regional tectonic stresses and plate movement [*Garcia et al.*, 2002; *Stefánsson et al.*, 2008] and low-magnitude seismic swarms (magnitude less than 3 M_w) that occur due to local dike intrusions or hydrothermal activity [*Hensch et al.*, 2007]. Elevated pore pressures are thought to prevail throughout the TFZ [*Stefánsson et al.*, 2008]. *Claesson et al.* [2004] observed distinct geochemical changes in thermal waters near the town of Húsavik at the eastern end of the TFZ before and after a magnitude 5.8 M_w earthquake in September 2002. Cu, Zn, Mn, and Cr levels showed statistically significant anomalies up to 10 weeks before the earthquake while other elements such as Na, Ca, K, $\delta^{18}O$ and δD showed significant changes between 2 to 9 days after the earthquakes. The chemical anomalies dissipated after two years and element concentrations and isotope ratios returned to their

[1]Steinmann Institute, Department of Geodynamics, University of Bonn, Bonn, Germany.
[2]Institute of Petroleum Engineering, Heriot-Watt University, Edinburgh, UK.
[3]School of Geosciences, University of Edinburgh, Edinburgh, UK.

0148-0227/11/2010JB007732

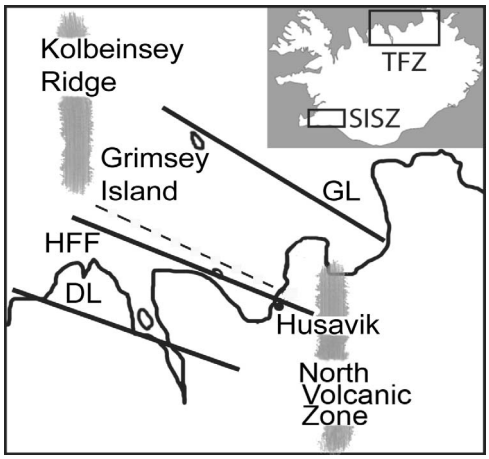

Figure 1. Map of the Tjörnes Fracture Zone and surrounding regions. The inset shows the locations of the South Iceland Seismic Zone (SISZ) and the Tjörnes Fracture Zone (TFZ). The Mid Atlantic Ridge is represented on land (North Volcanic Zone) and offshore (Kolbeinsey Ridge) by the wide gray shaded areas. The main geological structures in the TFZ are the Grimsey Lineament (GL), the Húsavik Flatey Fault (HFF) and the Dalvik Lineament (DL). The Tjörnes Peninsula is located between the Húsavik Flatey Fault and the Grimsey Lineament. The dashed line shows the direction of the seismic profile used in our simulations.

original preearthquake values [*Claesson et al.*, 2007]. It was speculated that variations in the stress field caused two aquifers to mix, with additional fluids leaking upwards from a deeper and hotter basaltic aquifer. Using high-resolution fluid flow simulations, *Lupi et al.* [2010] demonstrated that the natural large-scale flow system in the TFZ probably comprises two distinct regimes: a deep system with slow convective fluid flow in the basement and a shallow system with faster convection in the sedimentary basins. Both regimes are well separated and only very limited fluid exchange occurs between them along a small number faults, most notably at the eastern end of the TFZ where the geochemical anomalies were measured and hot waters are observed in the harbor of Húsavik. These two flow systems are only likely to mix due to a major external perturbation, i.e. if the local stresses change around a fault and cause the fault permeability to increase, for example during seismic pumping [*Sibson*, 1985]. This would allow fluids from the deeper flow regime to leak into the shallower one, thereby creating the distinct hydrogeochemical changes observed in Húsavik.

[4] The concept that seismicity affects not only hydrogeochemistry but also, more generally, fluid flow, is well established. Examples of postseismic changes in regional groundwater flow include variations in flow patterns within volcano-hydrothermal systems [*Manga and Brodsky*, 2006], temperature fluctuations in mid-ocean ridge black smoker vents [*Johnson et al.*, 2000], water level changes in deep wells [*Roeloffs et al.*, 2003], overpressure and earthquake-induced sediment failure at continental slopes [*Stigall and Dugan*, 2010], and variations in geyser periodicity [*Husen et al.*, 2004]. Such geological responses do not necessarily need to occur in the vicinity of an epicenter. Seismic waves can travel great distances and affect groundwater flow in far-field regions: induced microseismicity and pore pressure changes were observed in hot continental crust up to 1250 km away from the epicenter of the 7.2 M_w Landers earthquake in the western United States [*Hill et al.*, 2002]. On the other hand, the notion that elevated pore pressures, that is pore pressures above hydrostatic pressure, can lead to failure and induce seismicity because the effective stress on the material has changed was already recognized in the early work of *Terzaghi* [1923, 1925]. High pore pressures reduce the effective normal stress acting on a fault and cause movement along the fault plane (e.g., slip), which is accompanied by a sudden increase in fault permeability [*Rubey and Hubbert*, 1965; *Sibson*, 1990; *Rice*, 1992]. In these circumstances faults act as valves and allow fluids to migrate upwards in the crust at high rates [*Sibson*, 1990; *Rice*, 1992; *David et al.*, 1994; *Cox*, 1995; *Evans et al.*, 1997; *Wiprut and Zoback*, 2000; *Stanislavsky and Garven*, 2003; *Sibson*, 2007]. This can lead to the formation of solitary pressure waves because permeability variations due to changes in effective fault normal stress are usually a power law of porosity [*Rice*, 1992; *Revil and Cathles*, 2002]. Examples of induced seismicity include, but are not limited to, seasonal seismicity in volcanic areas [*Christiansen et al.*, 2005], production-induced seismicity due to high fluid injection rates [*Zoback and Zinke*, 2002], or the occurrence of pore pressure driven aftershock sequences [*Miller et al.*, 2004].

[5] Crustal permeabilities are generally assumed to decay exponentially as a function of depth, with bulk permeabilities of 10^{-16} to 10^{-17} m^2 between 4 and 10 km depth [*Manning and Ingebritsen*, 1999; *Saar and Manga*, 2004; *Jiang et al.*, 2010]. In intraplate regions, hydraulically conductive and critically stressed faults probably maintain these bulk permeabilities, which keeps pore pressures at hydrostatic levels and strengthens the crust [*Townend and Zoback*, 2000]. Recent theoretical studies [*Rojstaczer et al.*, 2008; *Ingebritsen and Manning*, 2010] lend further support and demonstrate that crustal permeabilities are constantly evolving due to internal and external forcing to maintain subcritical pore pressures. On the other hand, the close coupling between seismicity and fluid flow due to critically high pore pressures, that is pore pressures close to lithostatic pressure, in seismogenic zones continually weakens the rock by regenerating fracture-controlled permeability that decreases and increases over orders of magnitude locally and transiently [*Sibson*, 1992]. Recent field evidence also points to extreme fluid fluxes that may accompany such short-lived permeability increase [*Cox and Ruming*, 2004; *Okamoto and Tsuchiya*, 2009]. An elegant conceptual model behind this process is the toggle switch mechanism [*Miller and Nur*, 2000] where faults drive fluid-controlled seismic events. The toggle switch mechanism occurs in four phases: 1) fault zone compaction, 2) fluid pressure increase, 3) dilatant slip and/or fault inflation and 4) fault sealing (Figure 2).

[6] The aim of this study is to apply the concept of the toggle switch mechanism in a series of high-resolution simulations and model the four different phases outlined above. We use the TFZ, a prime example of critically pressured oceanic crust in a tectonically active hydrothermal system, as our case study and analyze the regional and local response of the preseismic, coseismic, and postseismic fluid

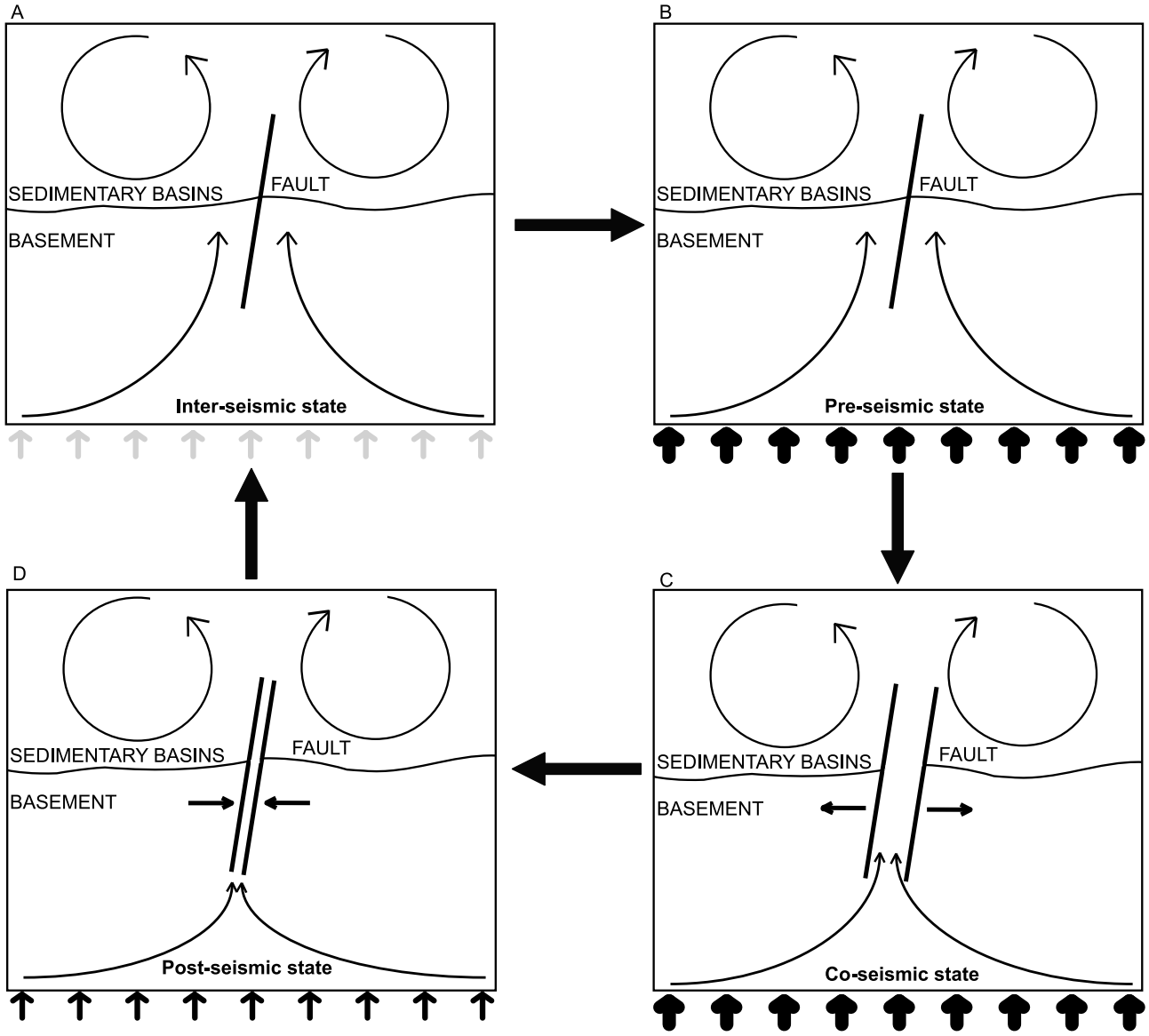

Figure 2. Conceptual picture of the toggle switch mechanism [*Miller and Nur*, 2000] as assumed to operate in the Tjörnes Fracture Zone. (a) The interseismic state shows two separated fluid flow regimes, one in the sedimentary basins, characterized by intense convection and one in the basement, characterized by much slower convection [*Lupi et al.*, 2010]. An increase in the rate at which volatiles migrate upwards due to mantle and magma degassing in the TFZ leads to the (b) preseismic state and causes elevated pore pressures in the fault and in the basement. The fault inflates during the (c) coseismic phase which is accompanied by a sudden increase in fault permeability that connects both flow regimes and mixes deep and shallow fluids. (d) During the postseismic state, the fluid pressure dissipates and the faults close due to a decrease of the pore pressure and volatile migration rate.

flow behavior. This allows us to address the following questions: 1) Are the hydrogeochemical variations observed before and after the September 2002 earthquake in the TFZ consistent with the flow processes thought to occur during the toggle switch mechanism? 2) How can critical pore pressures be generated and maintained in the TFZ and how are they distributed? 3) What are the timescales of a complete toggle switch cycle in the TFZ? 4) What is the nature of coseismic and postseismic fluid flow in the vicinity of a fluid-induced seismic event?

[7] To answer these questions, we solve the pressure diffusion equation for fluid flow in hydrothermal systems [*Geiger et al.*, 2006] coupled with a spatially and temporally varying permeability that evolves as a function of the effective fault normal stress [*Rice*, 1992]. This allows us to simulate how a fault inflates due to local changes in pore pressure. A high-resolution geological model [*Lupi et al.*, 2010] that is based on a seismic profile of the TFZ [*Gunnarsson*, 1998] with the initial pressure, temperature, and salinity distribution shown in Figure 3 was used in our

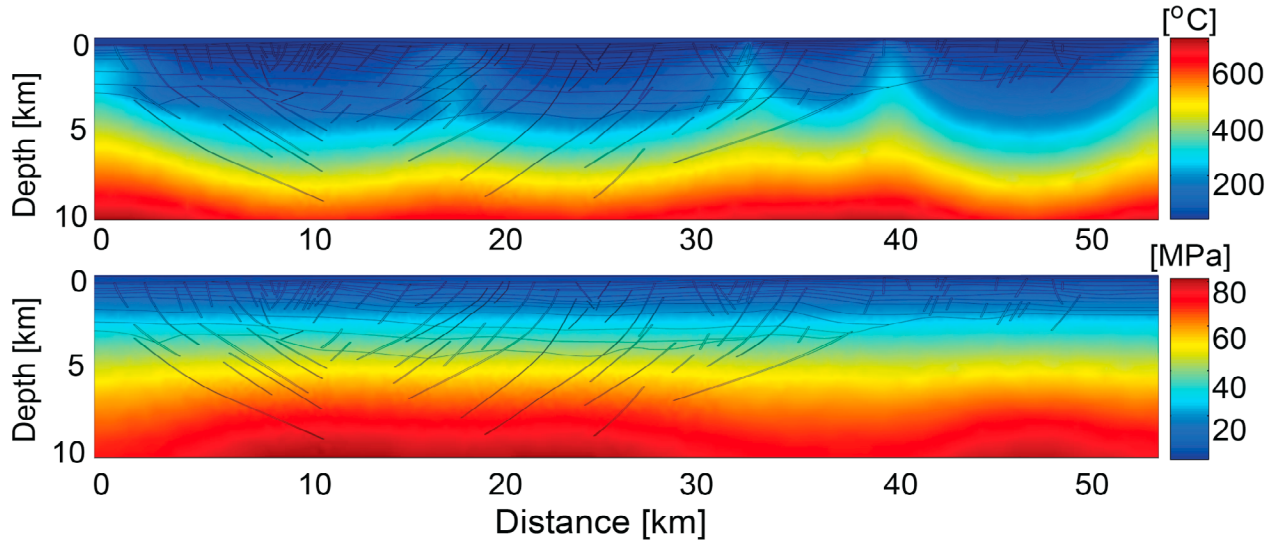

Figure 3. Initial temperature and fluid pressure distribution in the TFZ after approximately 0.9 Ma [*Lupi et al.*, 2010].

simulations (Figure 4). Our conceptual model is shown in Figure 2 and the workflow is summarized in Table 1. We model the four different phases of the toggle switch mechanism in sequential steps. We start with the interseismic state where fluid flow in the TFZ is characterized by two separated convective systems, one in the sedimentary basins and one in the basement [*Lupi et al.*, 2010]. During the preseismic state, mantle- and magma-derived volatiles (predominantly H_2O and CO_2) that migrate upwards in the deepest parts of the TFZ generate pore pressures which are locally above hydrostatic [*Nichols et al.*, 2002; *MacPherson et al.*, 2005; *Hensch et al.*, 2007; *Stefánsson et al.*, 2008]. During the coseismic and postseismic state, we allow fault permeabilities to change as a function of the evolving effective fault normal stress [*Rice*, 1992]. As a consequence, faults which originally comprise low permeabilities begin to inflate. This enhances their permeabilities and causes the faults to "unzip" themselves from bottom to top. This permeability increase allows pore pressures to dissipate. As a consequence, fluids from the deeper and hotter parts of the TFZ migrate upwards in the fault planes, connecting the deeper flow regime in the basement with the shallower flow regime in the sediments. During the late stages of the postseismic state, the permeability of the faults decays to its original value, which separates the two flow systems again.

[8] The paper is organized as follows. We first present the geology of the Tjörnes Fracture Zone. Then we describe the geological and mathematical model, including the key

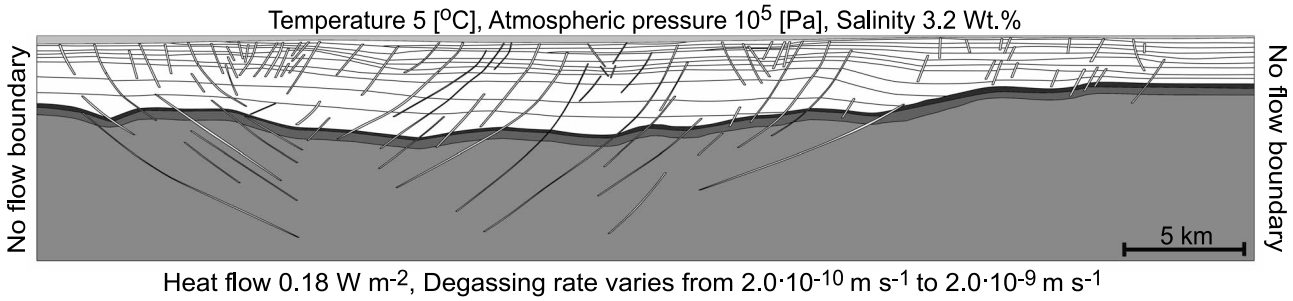

Figure 4. Model geometry, based on the interpretation of the seismic cross section by *Gunnarsson* [1998], and corresponding boundary conditions. The model consists of the sea (light gray area), 13 sedimentary layers (white area) and the top basement, middle basement and deep basement (dark, medium, and light gray areas, respectively). Here 86 faults have been identified in the seismic profile [*Rögnvaldasson et al.*, 1998] and are divided into shallow and deep faults, which range in width from 20 to 120 m. The left and right boundary are no-flow boundaries. The top boundary is characterized by constant values of temperature, pressure and salinity as shown. The bottom boundary accounts for a constant heat flow of 0.18 W m^{-2} and constant basal fluid flux. The impact of different basal fluid fluxes, ranging from 2.0×10^{-10} m s^{-1} to 5.4×10^{-9} m s^{-1}, is analyzed in the simulations.

Table 1. Summary of the Two Simulation Steps

Type of Simulation	Aim	Method
	Preseismic State	
Transient pressure diffusion	To evaluate the time required to reach a steady state pore pressure distribution in the TFZ	Different spatially and temporally constant mantle degassing rates are analyzed. They range from 2.0×10^{-10} m s^{-1} to 5.4×10^{-9} m s^{-1}
	Coseismic and Postseismic State	
Transient pressure diffusion	To evaluate the fluid flow behavior and the fault inflation during the coseismic and postseismic state	A high mantle degassing rate of 5.4×10^{-9} m s^{-1} is used, which leads to overpressure and fault inflation. The permeability is allowed to vary as a function of σ_n

assumptions. We then present the results and discuss how they relate to timescales of fluid flow in the TFZ and in other hydrothermal systems.

2. Geological Setting of the Icelandic Seismic Regions

[9] Seismic events in Iceland are frequent and mostly distributed along the Mid Atlantic Ridge [*Einarsson*, 1991; *Sigmundsson*, 2006]. The Tjörnes Fracture Zone (TFZ) and the South Iceland Seismic Zone (SISZ), generally described as transform zones [*Saemundsson*, 1974; *Bergerat et al.*, 2000; *Bergerat and Angelier*, 2007], are the seismically most active areas in Iceland. They offset segments of the Mid Atlantic Ridge and are characterized by low-and high-magnitude seismic events. The TFZ is located between the Kolbeinsey Ridge and the North Volcanic Zone (Figure 1) and comprises sedimentary and magmatic lithologies [*Riedel et al.*, 2005]. Overall it is a transtensional fracture zone where 500 to 4000 m deep sedimentary basins are filled with marine and glacial-related sediments [*Richter*, 2006; *Gunnarsson*, 1998]. The shallower parts of the Tjörnes basins crop out in the Tjörnes peninsula (Figure 1). They consist, from base to top, of Tertiary lava flows which are overlain by a sequence of sedimentary layers up to 500 m thick [*Richter*, 2006]. Above these units a Pliocene lava succession alternating with marine sedimentary lithologies occurs. On top of these Pliocene lava flows, tills, and other glacial origin sediments occur [*Richter*, 2006]. The upper part of this succession has also been found on the Flatey Island (Figure 1) approximately 15 km offshore of Húsavik in a 600 m deep borehole. This implies lateral continuity, at least for the shallow sediments. Below the sedimentary basins, picritic rocks occur in the basement up to 5 km depth while gabbroic rocks characterize the deep oceanic crust [*Riedel et al.*, 2005]. Below the gabbroic bodies a MgO rich mantle is present [*Riedel et al.*, 2005]. This mantle is generally considered to be wet [*Nichols et al.*, 2002], causing the release of volatiles (mostly H_2O and CO_2 with minor amounts of noble gases) below the TFZ [*MacPherson et al.*, 2005]. Further volatile contributions come from magmatic intrusions in the TFZ [*MacPherson et al.*, 2005], such as dikes [*Hensch et al.*, 2007]. Upward migration of these volatiles is thought to lead to elevated pore pressures in the deeper parts of the TFZ [*Stefánsson et al.*, 2008].

[10] The intense faulting of the TFZ and, in particular, the formation of the sedimentary basins has been related to the tectonic regime [*Gudmundsson*, 2007]. *Saemundsson* [1974] and *Bergerat et al.* [2000] identified three tectonic regimes in the regional geodynamic setting: dextral ENE–WSW trending transtension, NE–SW Húsavik Flatey Fault-perpendicular extension, and a NW–SE Húsavik Flatey Fault-parallel extension [*Garcia et al.*, 2002]. Although the overall tectonic regime of the TFZ can be defined as transtensional, flower structures, characteristic of compressional regimes, also occur locally. A large rollover structure, with amplitude and wavelength of approximately 1 km and 10 km, respectively, is apparent in the TFZ close to the Kolbeinsey ridge [*Richter*, 2006]. Several synthetic and antithetic listric faults, associated with a crustal-scale listric fault dipping toward the southwest, are present in the TFZ [*Richter*, 2006]. The main geological structures of the TFZ, the Húsavik Flatey Fault, the Grimsey Lineament, and the Dalvik Lineament, are characterized by abundant seismic activity [*Stefánsson et al.*, 2008]. Microseismicity is intense and occurs mainly between 2 and 10 km depth but never below 16 km [*Rögnvaldasson et al.*, 1998]. *Stefánsson et al.* [2008] suggest that this may be caused by elevated pore pressures that migrate upwards from the ductile crust across the brittle-ductile transition toward shallow depths. Low-magnitude events (up to 4.0 M_w), are caused by variations of the local stress fields [*Rögnvaldasson et al.*, 1998; *Garcia et al.*, 2002]. These variations are generated by dike intrusions, hydrothermal fluid flow, and deep fluid migration across the brittle-ductile transition [*Hensch et al.*, 2007; *Stefánsson et al.*, 2008]. High-magnitude earthquakes (up to 7.0 M_w), caused by the regional tectonic forces [*Garcia et al.*, 2002], have been recorded in the area over the last century [*Stefánsson et al.*, 2008].

3. Model Description

3.1. Geometrical Modeling

[11] Our geological model [*Lupi et al.*, 2010] is based on the interpretation of a seismic profile of the TFZ [*Gunnarsson*, 1998] (Figure 4). It has been extended up to 10 km depth in order to include the likely position of the brittle-ductile transition. We reproduce 13 sedimentary layers, 86 faults (shallow and deep) and the basement (separated into top, middle and deep). The faults are reproduced as high aspect ratio structures with widths generally varying from 20 m to 120 m but also up to 500 m for large damaged areas. Geological unconformities, lens-shaped sedimentary layers, and layering offset by faulting are also reproduced. A computer-aided design (CAD) geometry was built [*Paluszny et al.*, 2007] and discretized into approximately 50,000 adaptively

refined triangular finite elements using the commercial software ANSYS ICEM™.

3.2. Conceptual Model

[12] Our key conceptual model is that the feedback between fluid flow, pore pressure diffusion, and permeability evolution in the TFZ can be described by the toggle switch mechanism [*Miller and Nur*, 2000] (Figure 2). Hence we study the different phases of the toggle switch mechanism in our simulations using two separate steps. These are summarized in Table 1. The first simulation step models the preseismic state. We start with a single representative pore pressure, temperature and salinity distribution (hereafter referred to as P-T-X distribution) for the TFZ [*Lupi et al.*, 2010]. The P-T-X distribution was obtained by simulating the regional fluid flow in the TFZ for a time of approximately 1 Ma. At this time, the two distinct flow regimes, which separate fluid flow in the basement from fluid flow in the sedimentary basins, already exist. High-permeability faults may connect the two flow regimes temporarily, causing two chemically distinct fluids to mix, which generates the distinct shift in hydrogeochemistry observed by *Claesson et al.* [2004, 2007]. As shown by *Lupi et al.* [2010], the large-scale flow pattern in the TFZ is not stationary over time and individual upflow zones of hot hydrothermal fluids continue to migrate slowly. Since the separation into two flow regimes exists throughout, the 1 Ma snapshot taken here is thought to be a representative P-T-X distribution that captures the key flow processes in the TFZ.

[13] Seismic data appears to be consistent with the occurrence of elevated pore pressures at depth; volatiles leaving the brittle-ductile boundary and migrating upwards are thought to cause the elevated pore pressures [*Stefánsson et al.*, 2008]. Geochemical analysis of basaltic glasses from Iceland shows that the mantle is wet, i.e. it has a significantly elevated water content, which degasses from the mantle [*Nichols et al.*, 2002]. $^3He/^4He$ ratios show that the source of volatiles in the TFZ is the mantle with additional contributions of volatiles degassing from magmatic intrusions [*MacPherson et al.*, 2005]. Intrusions include shallow dikes [*Hensch et al.*, 2007] and, possibly, partially molten basalts at 10 to 15 km depth [*Stefánsson et al.*, 2008]. The volatiles consist mainly of H_2O and CO_2 but include small amounts of noble gases as well [*MacPherson et al.*, 2005]. We simulate the volatile degassing from depth by applying a spatially and temporally constant fluid flux at the bottom boundary of our model. Since the exact rates of mantle and magma degassing and the physical nature of volatiles (gases, liquids, or supercritical fluids) are unknown, we investigate the effect of different fluxes in separate simulations. The fluxes range from 2.0×10^{-10} m s^{-1} to 5.4×10^{-9} m s^{-1}. Note that because the ratio of mantle versus magma degassing is unknown as well, we combine both processes in a single rate termed "mantle degassing" or "basal fluid flux" in the following; this represents the volumetric flux of mantle- and magma-derived volatiles per unit area traveling upwards into the basement of the TFZ. Mantle degassing causes an enhancement of the upward fluid flow through the basement, lower crust, and faults. This leads to an increase in pore pressures inside the faults and in the deep parts of the crust. The results of this first step, the preseismic state, provide the initial pore pressure distribution in the TFZ and form the basis for the second simulation step that models the coseismic and postseismic state.

[14] In this second step we consider only a basal fluid flux rate of 5.4×10^{-9} m s^{-1}, as discussed further below. In contrast to the first step, we now allow the permeability of the faults to vary as function of the evolving stress. The increase in fault permeability with decreasing effective fault normal stress models the inflation of a fault, which "unzips" itself from bottom to top to release the elevated pore pressure. However, this process does not model the dilatant slip of the fault itself that may occur during a seismic event. High fault permeabilities are retained as long as the pore pressures remain elevated inside the faults. As the local fluid flux decreases with time, the effective fault normal stress changes locally and the permeability of the faults returns to their original values as the faults deflate.

3.3. Mathematical Formulation

[15] By combining the mass conservation equation for compressible fluids

$$\phi \frac{\partial \rho_f}{\partial t} = -\nabla \cdot \left(\mathbf{v_f} \rho_f\right) + Q \tag{1}$$

with the momentum conservation equation given by Darcy's law

$$\mathbf{v_f} = -\frac{k}{\mu_f}\left[\nabla P_f - \rho_f \mathbf{g}\right] \tag{2}$$

it is possible to derive the pressure diffusion equation for hydrothermal fluids [*Geiger et al.*, 2006]

$$\rho_f \beta_t \frac{\partial P_f}{\partial t} = \nabla \cdot \left[\left(\frac{k}{\mu_f}\rho_f\right)\nabla P_f\right] - \nabla \cdot \left[\frac{k}{\mu_f}\rho_f^2 \mathbf{g}\right] + \rho_f \phi \left[\gamma_f \frac{\partial X}{\partial t} - \alpha_f \frac{\partial T}{\partial t}\right] + Q, \tag{3}$$

which we solve using an implicit finite element method. Here ϕ is the porosity (assumed to be constant), ρ_f the fluid density, $\beta_t = (1 - \phi)\beta_r + \phi\beta_f$ is the total compressibility of the fluid, f, and rock, r, system, $\mathbf{v_f}$ the Darcy velocity, k the permeability (assumed to be a scalar), μ_f the fluid viscosity, P_f the pore pressure and $\mathbf{g}$ the vector of gravitational acceleration. k, ϕ, β_r, and $\mathbf{v}_f$ are piecewise constant properties stored at the finite elements. P_f as well as all fluid properties (e.g., μ_f, ρ_f) are properties stored at the nodes of the finite element mesh and extrapolated to the finite elements where needed. The source term Q in equations (1) and (3) represents the basal fluid flow (or "mantle degassing rate"). X is the salinity and T the temperature of the hydrothermal fluids. α_f and γ_f are the thermal expansivity and chemical expansivity of the fluid, respectively. We treat the system as isothermal and isochemical and consider $\frac{\partial T}{\partial t}$ and $\frac{\partial X}{\partial t}$ to be zero. ρ_f, μ_f as well as α, β and γ are computed from an equation of state for H_2O–NaCl fluids [*Driesner and Heinrich*, 2007; *Driesner*, 2007] during each time step. Note that via the rock compressibility β_r this model accounts for compaction of the rock due to pore pressure changes. Although in this idealized approach β_r does not include the full poroelastic theory, it is still a viable model in this instance because β_r is usually several orders of magnitude smaller than the fluid compressibility β_f of hydrothermal fluids [*Geiger et al.*, 2006].

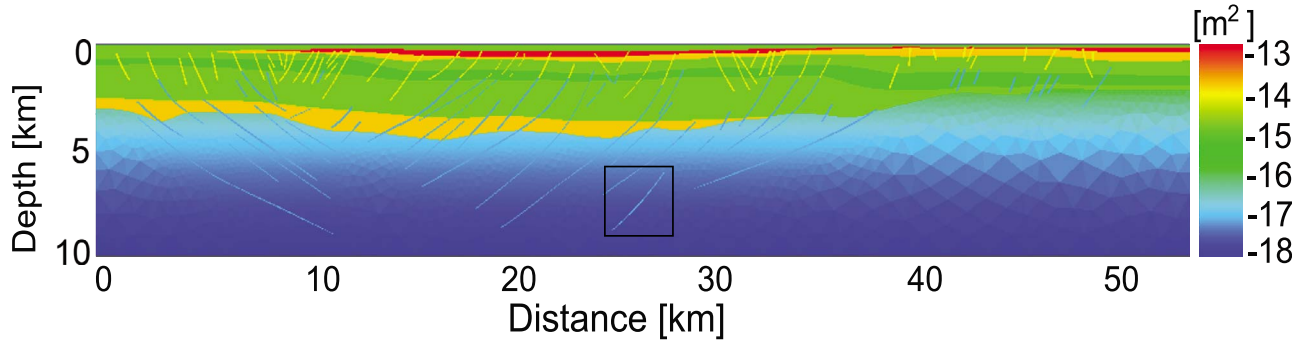

Figure 5. Permeability distribution of the Tjörnes Fracture Zone during the interseismic and preseismic state after *Lupi et al.* [2010]. The permeability of the deep faults and basement varies with depth according to equation (4) (see Table 2 for values of k_0). The black box shows the location of the fault depicted in Figure 12. Note that the checkered pattern is caused by visualizing the element-wise constant permeabilities on an unstructured finite element mesh.

3.4. Timescales and Boundary Conditions

[16] The time window for each simulation step varies. The first set of simulations that model the preseismic state are run for ~4.5 kyrs to ensure that the system reaches a steady state pore pressure distribution. In order to capture the pore pressure buildup adequately, we applied time steps (Δt) of 1 yr. The second simulation step considers much shorter timescales from a few minutes to a few years. This was necessary to resolve flow processes that occur very quickly, i.e., coseismic fluid flow and postseismic permeability decay. Simulations lasting for less than 24 hours are based on fixed time steps of minutes. Simulations lasting for more than 24 hours but less than two years use fixed time steps of hours, otherwise we use time steps of months. For each simulation we reduced the time step in multiple trial runs until a stable numerical result was obtained. This time step was then used in the subsequent simulations.

[17] The model geometry and boundary conditions are shown in Figure 4. The right and the left model boundaries are no-flow boundaries while the top boundary is at sea level. We assign a fixed temperature of 5°C, a fixed pressure of 1.0×10^5 Pa, and a fixed salinity of 3.2 Wt.% to the top boundary. The hydrostatic pressure acting on the seafloor varies according to the depth of the sea which is given by the seafloor topography.

3.5. Heat Flow and Fluid Flux at the Bottom Boundary

[18] We use a uniform basal heat flow of 0.18 W m^{-2} in both simulation steps, which is relatively well constrained in the TFZ [*Flóvenz and Saemundsson*, 1993; *Flóvenz*, 2008; *Lupi et al.*, 2010]. To the best of our knowledge, there are no direct measurements of the rates at which H_2O and CO_2 degas from mantle and magma in the TFZ. We hence test the model sensitivities for different spatially and temporally constant basal fluid fluxes. They range from 2.0×10^{-10} m s^{-1} to 5.4×10^{-9} m s^{-1}. These values include both, mantle and magma degassing rates as noted above. The upper value is slightly higher than the average surface degassing rate of 2.0×10^{-9} m s^{-1} measured in the South Iceland Seismic Zone [*Fridriksson et al.*, 2006]. However, this value is not unreasonable considering the presence of shallow dikes [*Hensch et al.*, 2007] and possibly molten basalts between 10 and 15 km depth [*Stefánsson et al.*, 2008] in the Tjörnes peninsula, which both contribute to the volatiles released from the wet Icelandic mantle [*Nichols et al.*, 2002; *MacPherson et al.*, 2005]. This may cause, at least locally, higher volatile fluxes.

3.6. Permeability Modeling

3.6.1. Preseismic State

[19] For the preseismic state, we use the permeability values of *Lupi et al.* [2010] to characterize the hydrostratigraphy of the TFZ. Figure 5 shows the permeability distribution used for this set of simulations. In general, shallow faults and the upper basement have constant permeabilities. The permeability of the sedimentary layers decreases with depth, mimicking older and more compacted rocks. We characterized the damaged zone of the shallow faults with a permeability of 5.0×10^{-14} m^2. The time-averaged permeability of the deeper basement and of the deep faults is modeled by the relation [*Manning and Ingebritsen*, 1999]

$$\log_{10}(k) = \log_{10}(k_0) - 3.2 \log_{10}(z) \quad (4)$$

where k_0 is the permeability in [m^2] at 1 km depth and z denotes the depth in [km]. *Manning and Ingebritsen* [1999] used $k_0 = 10^{-14}$ m^2 for the continental crust. We varied k_0 depending on the lithology (Table 2).

Table 2. Parameters Used During the Two Simulation Steps[a]

Geological Unit	k (m^2)	k_0 (m^2)	$\hat{k}_0$ (m^2)	ϕ (-)	σ^* (MPa)	ρ_r (kg m^{-3})
Shallow faults	3×10^{-14}	–	10^{-10}	0.22	10	2800
Deep faults	–	2×10^{-14}	10^{-10}	0.02	10	2800
Sediment basins	10^{-13} to 10^{-16}	–	3×10^{-13}	0.25 to 0.10	15	2600 to 2800
Basement	–	10^{-14}	3×10^{-14}	0.02	50	3000 to 3200

[a]Here k, k_0, ϕ, and ρ_r after *Lupi et al.* [2010], σ^* after *Miller et al.* [2004] (faults) and *David et al.* [1994] (basement and sediments).

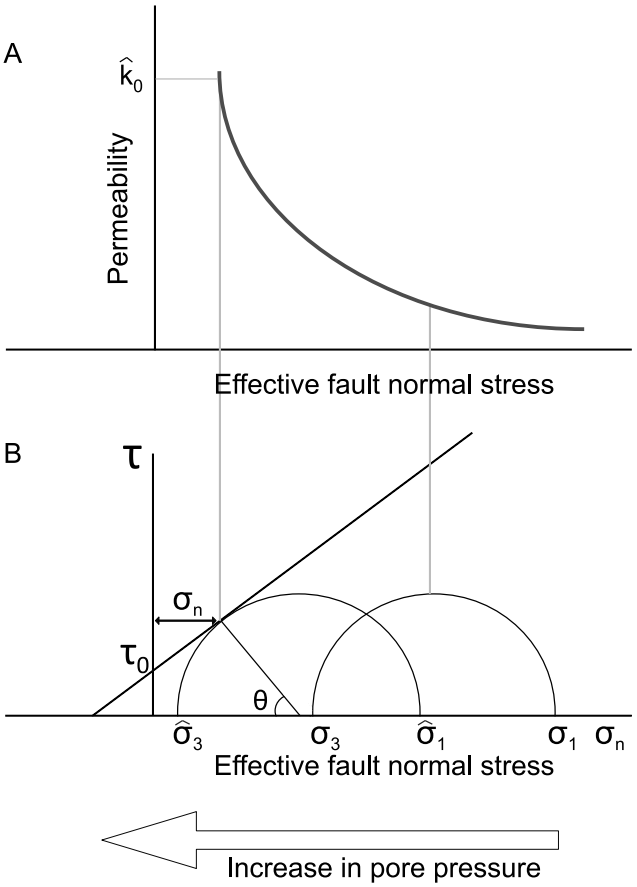

Figure 6. (a) Conceptual sketch showing the relation between permeability k and the effective fault normal stress σ_n, which is a function of the pore pressure P_f, see equations (5) and (6). (b) The Mohr circle shows how an increase in pore pressure reduces σ_1 and σ_3 to σ_1 and σ_3, respectively. It causes a decrease in effective fault normal stress and an exponential increase in permeability up to the maximum value $\hat{k}_0$ when the fracturing threshold is reached. This models fault inflation due to local changes in pore pressure. Figure 7 shows the actual $k - \sigma_n$ relation used in the simulations.

3.6.2. Coseismic and Postseismic State

[20] When the pore pressure inside the fault increases, the effective fault normal stress decreases locally and the fault inflates, i.e. its permeability increases. We model this effect in the second simulation step by allowing the permeability of the faults to vary as a function of the effective fault normal stress σ_n which is a function of the pore pressure P_f [*Rice*, 1992]

$$k = \hat{k}_0 \exp \frac{-\sigma_n(P_f)}{\sigma^*}, \tag{5}$$

where $\hat{k}_0$ is the permeability at zero effective fault normal stress. Note that although this model has been successfully used to model fault permeability changes as a function of the effective fault normal stress [*Revil and Cathles*, 2002; *Miller et al.*, 2004; *Crutchley et al.*, 2010], it does not account, strictly speaking, for dilatant slip or hydraulic fracturing which can occur when the pore pressure exceeds the lithostatic load [*Sibson*, 1974, 1981]. The characteristic stress σ^* [*Rice*, 1992; *David et al.*, 1994; *Revil and Cathles*, 2002; *Miller et al.*, 2004] is a constant that expresses the degree of fracturing of a geological structure. σ^* is equal to the reciprocal of the pressure sensitivity coefficient and can be measured in laboratory experiments [*David et al.*, 1994] or by fitting field data [*Henry*, 2000]. Lower values of σ^* correspond to highly fractured rocks [*Rice*, 1992; *Miller et al.*, 2004]. We use the data of *David et al.* [1994] with $\sigma^* = 50$ MPa for the unfractured (picritic) basement and $\sigma^* = 15$ MPa for the (unfractured) sediments. For the faults we use the same values as *Miller et al.* [2004], that is $\sigma^* = 10$ MPa. The conceptual model of the permeability–pore pressure relation given by equation (5) is shown in Figure 6. The actual permeability–pore pressure relations used for the faults, basement, and sedimentary basins are shown in Figure 7.

[21] The effective fault normal stress is given by *Ingebritsen et al.* [2006]

$$\sigma_n = \frac{\sigma_1 + \sigma_3 - 2P_f}{2} + \frac{\sigma_1 - \sigma_3}{2}\cos 2\theta, \tag{6}$$

where σ_1 and σ_3 are the largest and least principal stresses acting on the fault, respectively, and θ is the dip angle of the fault (Figure 6). The complex tectonic state of the Tjörnes Fracture Zone is characterized by the interplay of transtensional and extensional stress regimes [*Saemundsson*, 1974; *Gudmundsson*, 1993; *Garcia et al.*, 2002]. We assume an extensional regime where σ_1 is vertical, i.e. equal to the lithostatic load $\sigma_v = \int_0^z \rho_r g dz$, where ρ_r is the rock density and g is the gravitational constant. For an idealized extensional regime we then take $\sigma_3 = 0.7 \times \sigma_1$ [*Miller et al.*, 2004; *Jaeger et al.*, 2007; *Peng and Zhang*, 2007] and $\theta = 40°$ [*Zoback et al.*, 2003; *Jaeger et al.*, 2007]. σ_3 is oriented in the plane of Figure 4, i.e. the faults strike perpendicular to

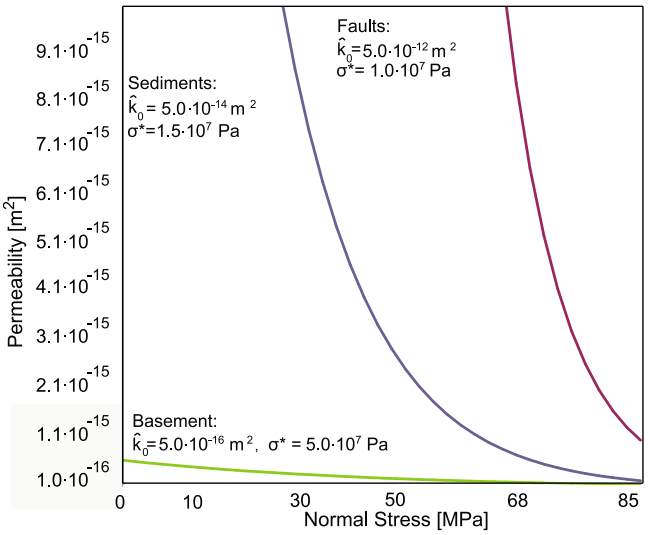

Figure 7. Permeability decay as function of effective fault normal stress σ_n, permeability threshold $\hat{k}_0$, and characteristic stress σ^* for faults, sedimentary layers, and basement (equation (5)). The pore pressure varies between hydrostatic and lithostatic at 8 km depth.

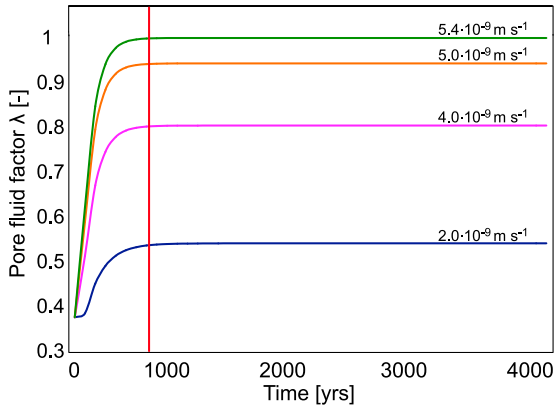

Figure 8. Buildup of pore fluid factor $\lambda = P_f/(\sigma_v + \tau)$ at 9.9 km depth for different mantle degassing rates. The vertical line represents the time after which the pore pressure does not change any longer.

σ_n. We also tested for a strike-slip tectonic setting with σ_2 being vertical, $\sigma_1 = 1.1 \times \sigma_v$, $\sigma_3 = 0.625 \times \sigma_1$, and $\theta = 55°$ but observe no major impact on the results as discussed below.

[22] The pore fluid factor λ relates the pore pressure P_f to σ_v and the tensile strength τ as [*Sibson*, 1974]

$$\lambda = \frac{P_f}{\sigma_v + \tau}, \tag{7}$$

which provides a simple measure as to how close the pore pressure is to inducing a fracture, assuming that the maximum strength of the rock can be approximated as the sum of lithostatic and tensile strength of the rock. We further define $\lambda^* = P_f/\sigma_v$, which is a measure of how close the pore pressure is to lithostatic pressure. For negligibly small tensile strength, e.g. in the deeper parts of the TFZ, $\lambda^* \approx \lambda$. Rocks fracture hydraulically the latest if $\lambda \geq 1$ but probably, as in the extensional regime considered here, at values of $\lambda < 1$. For example, *Rojstaczer et al.* [2008] propose that failure can occur if $\lambda^* \sim 1.5$. Since the exact value for λ^* where hydraulic fracturing can occur is difficult to establish, we use $\lambda \geq 1$ because it represents the upper limit when this must occur. We note that the resulting flow dynamics will not be affected by the choice of λ or λ^*,which only serve to "label" the area where excess pressure occurs. The exact values for τ, ρ_f, σ^* and $\hat{k}_0$ that we have used in the simulations are given in Table 2.

3.7. Key Assumptions

[23] Several assumptions and simplifications have been made to run the simulations at reasonable computational costs. We assumed that all rock parameters (i.e. k, k_0, ϕ, τ, ρ_r, σ^* and $\hat{k}_0$) are constant in time during the preseismic state. We only allow the permeability to vary as a function of σ_n, i.e. spatially and temporarily, during the coseismic and postseismic states. This is obviously incorrect for the porosity ϕ, which will also vary as rocks deform. However, this is still a reasonable assumption since, according to the cubic law [*Snow*, 1968], a change in fracture aperture, driven by the change in σ_n, affects the fluid fluxes cubically but porosity only linearly. Hence it is the orders of magnitude change in permeability k as a function of σ_n, not the relatively moderate change in porosity ϕ, that will dominate the flow behavior and can lead to wave-like propagation of the pressure front [*Rice*, 1992; *Revil and Cathles*, 2002]. This behavior is reflected in the exponential growth of permeability as a function of effective fault normal stress (equation (5)).

[24] We assume that the system is isothermal and isochemical over the short time period modeled because the pressure front travels much faster than the temperature front, which is retarded due to lower thermal diffusivities and heat exchange between fluid and rock. A change in salinity causes only a relatively small change in volumetric expansion, i.e. γ in equation (3) is comparatively small [*Geiger et al.*, 2005]. In addition, our earlier work demonstrated that salinity and temperature gradients in the vicinity of faults in the TFZ are probably small [*Lupi et al.*, 2010] and hence will not cause major volume changes when fluids travel upwards in the fault, which could affect the pore pressure. Another simplification is that our equation of state [*Driesner and Heinrich*, 2007; *Driesner*, 2007] does not account for CO_2. Equations of state for NaCl-H_2O-CO_2 fluids [*Spycher et al.*, 2003; *Spycher and Pruess*, 2005] are only available for low temperatures and pressures and not applicable to the extreme P-T-X conditions encountered in high-temperature and seismically active hydrothermal systems. However, as long as there is no free CO_2 phase in the TFZ, our equation of state still provides adequate fluid properties because NaCl has a greater impact on fluid density and viscosity than dissolved CO_2.

[25] The boundary conditions are assumed to be uniform and constant in time and space. We also consider the variation of heat flow, sediment compaction, and seafloor morphology with time as negligible because of the short time window used in our simulations. The lack of temporal and lateral variations of heat flow and mantle degassing rate across the lower boundary are rather notable simplifications. Changes in basal fluid flux are likely to occur locally, for example due to the intrusion of a dike at depth [*Hensch et al.*, 2007]. We also do not account for fault/fracture sealing due to precipitation of mineral phases which may increase the rate at which the permeability decays [*Lowell et al.*, 1993].

[26] An important simplification is that we use a 2D cross section. By doing this, we oversimplify the complex interplay of three-dimensional stresses acting on the faults. They probably vary locally between compressional, extensional, transpressional, and transtensional regime, particularly in a complex tectonic setting like the TFZ which underwent changes in tectonic regimes over time [*Saemundsson*, 1974; *Garcia et al.*, 2002]. Hence we only simulate the two end-member cases, extensional and strike-slip, as noted above. It is also not possible to simulate multiple seismic events occurring in the fault planes (e.g. seismic swarms) in our 2D simulations.

4. Results

4.1. Preseismic State

[27] Figure 8 shows the pore pressure buildup at 10 km depth where the permeability of the basement is approximately 2.0×10^{-17} m^2. While the maximum values of the

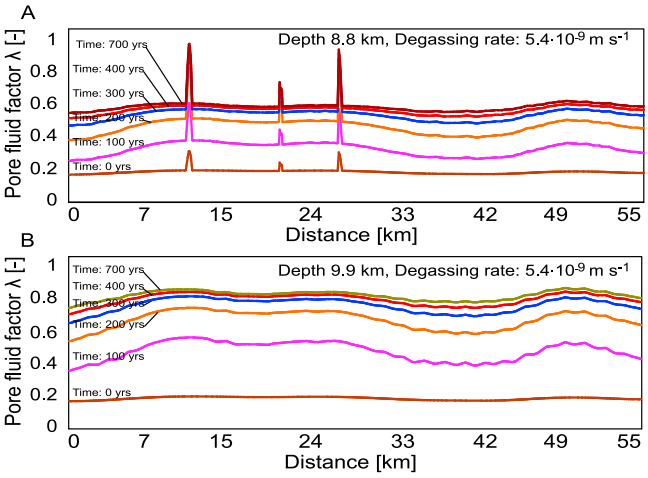

Figure 9. Pore fluid factor λ distribution along a horizontal profile at (a) 8.8 km depth and (b) 9.9 km depth at different times. A large pore pressure increase occurs within the first 300 years. Afterwards the buildup is slower. The peaks in Figure 9a represent three faults which reach 8.8 km depth. The faults have pore pressures close to lithostatic conditions, resulting in $\lambda \approx 1$. The variations in Figure 9b are caused by lateral variations in hydrostatic fluid pressure (Figure 3b).

pore pressure are a function of the mantle degassing rate and permeability, the time required to obtain a steady state pore pressure distribution does not vary. Maximum pore pressures are reached after approximately 700 years and result in values for λ of 0.55 for a mantle degassing rate of 2.0×10^{-9} m s^{-1} and $\lambda \approx 1$ for a mantle degassing rate of 5.4×10^{-9} m s^{-1}.

[28] Figure 9 shows the increase in pore pressure along two different horizontal profiles at 8.8 km and 9.9 km depth, respectively, as a function of time. The buildup is characterized by a fast increase during the first 300 years, followed by a slower increase lasting for another 400 years, after which the maximum pore pressure is reached. Figure 9a shows that the pore pressure at 8.8 km exhibits three prominent peaks. These peaks represent the elevated pore pressure inside faults with λ being close to 1. Additional simulations where we varied the tensile strength of the faults from 2 MPa to 10 MPa yield similar results. This indicates that the permeability contrast between faults and host rocks, not tensile strength, controls the increase in pore pressure and its local distribution. Figure 9b shows that pore pressure variations at 9.9 km depth are only minor. These smooth horizontal variations are related to the original pore pressure distribution. Due to the convective nature of the regional fluid flow in the TFZ, zones with higher hydrostatic pressures occur in areas where cold and dense fluids sink downward (Figure 3). This causes the local and less prominent variations in pore pressure and λ at larger depths.

[29] The pore pressure distribution in the TFZ immediately before the coseismic state, i.e. before the faults begin to inflate, is shown in Figure 10. Once the pore pressure reaches a steady state, it is possible to distinguish at least four main regions where elevated pore pressures occur. The deep crust comprises high pore pressures ($\lambda \approx 0.85$), which gradually decrease toward the upper structural levels of the basement. At depth, the fluids are focused into the faults, causing values of λ close to 1 (i.e. critically high pore pressures) in the deeper parts of the faults (Figure 9a). Lower pore pressure values, with λ between 0.5 and 0.15, are present between 7.5 km depth and the top of the basement. The sedimentary basins are characterized by low pore pressures and λ between 0.3 and 0.5. The shallow crust, less than 1 km below the seafloor, has values of $\lambda \approx 0.15$. These values are well below the lithostatic pressure but they can reach up to 1.2 times the hydrostatic pressure, which probably does not induce hydrofracturing in the TFZ (Figure 11).

4.2. Coseismic and Postseismic State

[30] Starting from the steady state pore pressure distribution (Figure 10), we now allow the permeability to vary as a function of the effective fault normal stress (equation (5)) and simulate fault inflation during the toggle switch mechanism (Figure 2c). The resulting pore velocities (i.e. $\mathbf{v_f}/\phi$, the rate at which a nonreactive solute travels through porous media), pore pressures and coseismic and postseismic fault permeability evolution are presented here.

[31] Figure 12 shows the pore pressure evolution along a 3.5 km long fault whose location is indicated by the inset black square in Figure 5. Horizontal profiles across the fault

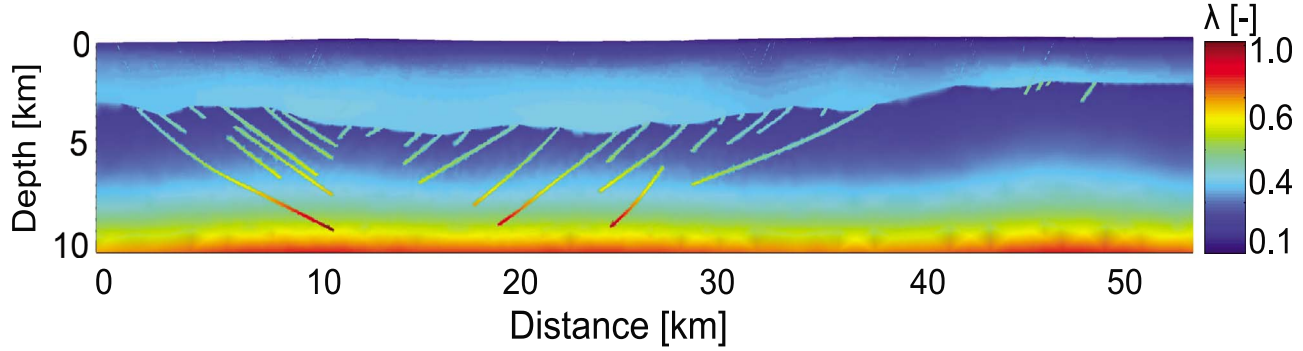

Figure 10. Pore fluid factor λ distribution before fault inflation and permeability increase. The permeability of the basement varies as given in equation (4), with $k_0 = 10^{-14}$ m^2 and a basal fluid flux of 5.4×10^{-9} m s^{-1}. The faults show higher pore pressures than the surrounding rocks, resulting in locally higher λ values.

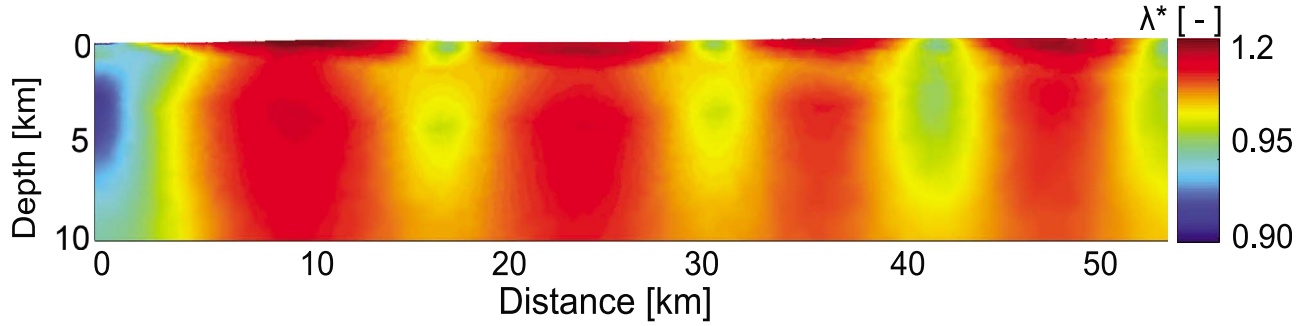

Figure 11. Distribution of the ratio of fluid pressure to hydrostatic pressure, $\lambda^* = P_f/\sigma_v$. The basal fluid flux and permeability model is identical to Figure 10.

are presented for pore pressure (Figure 13), pore velocity (Figure 14), and permeability (Figure 15). The location of the profiles is indicated by the black line in Figure 12a (for Figures 14 and 15) and Figure 12f (for Figures 13and 16), respectively. These lines are not to scale and only indicate the location across the fault. However, Figures 13, 14, 15, and 16 show the correct length of the horizontal profiles.

[32] Figure 12 shows how a fault inflates and unzips itself to release excess pore pressure. This occurs in the deeper part of the fault where λ is approximately 1 (Figure 12a). Pore pressure dissipates and λ falls below 0.85 after one minute (Figure 12b). Pore pressures continue to decrease (Figures 12c and 12d) in the deeper parts of the fault but also begin to build up in the upper parts of the fault (Figure 12e) because excess fluid travels upwards in the fault and cannot be released quickly enough into the basement. After 6 hours, values of λ close to 1 are reached at the top of the fault (Figure 12f). The pore pressure buildup in this region is shown in Figure 13. It increases rapidly during the first hour, followed by a slower buildup until values of λ close to 1 are reached. The fault permeability is enhanced but elevated pore pressures are maintained because the fault is confined within the low permeability basement. This prevents the pore pressure from diffusing fast enough from the fault into the basement. The high values of σ^* in the basement, which imply that the basement is mechanically stronger, cause the permeability to remain at lower values for longer time. However, pressure diffusion between fault and basement is clearly visible in Figures 12e and 12f by the expansion of a green halo, which represents values of $\lambda \approx 0.5$, away from the fault.

[33] Coseismic pore velocities are shown in Figure 14. The highest velocities (up to 0.03 m s^{-1}) are observed within the first minute after fault inflation occurs and maintained for five minutes. Afterwards they rapidly decrease, reaching minimum values of approximately 0.004 m s^{-1} after one

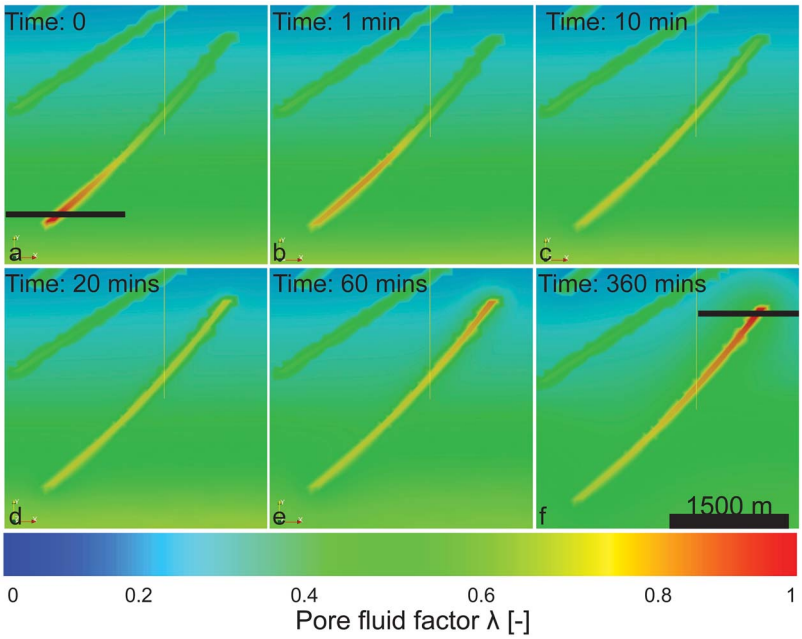

Figure 12. Coseismic pore fluid factor evolution in the fault shown by the black box in Figure 5. After permeability enhancement, pore pressures within the fault decrease and move upwards where they accumulate at the top of the fault, resulting in the upwards migration of the maximum λ values. The horizontal line in Figure 12a shows the locations of Figures 14 and 15 while the line in Figure 12f shows the locations of Figures 13 and 16.

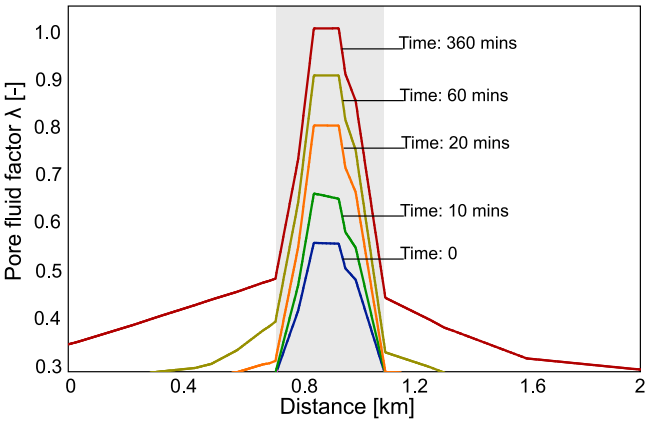

Figure 13. Buildup of the pore fluid factor λ in the fault depicted in Figure 12f at 6.1 km depth. The jagged lines are artifacts due to interpolating across the unstructured finite element grid. The gray shaded area shows the variation of λ within the fault zone.

hour. The high pore velocities are associated with the sudden coseismic change in fault permeability. Figure 15 shows how the initially low permeability of the fault and basement increases suddenly during the first minute of the coseismic state. The preseismic permeability contrast between basement and fault is one order of magnitude. After the fault starts to inflate, the permeability increases up to almost seven orders of magnitude, from ~3.0×10^{-16} to ~8.0×10^{-10} m^2. During the postseismic state, the permeability decreases with time to its preseismic values as the elevated pore pressure dissipate and σ_n increases. The rate of permeability decay is a function of σ^* and $\hat{k}_0$ (Figure 7) and hence the permeability of the fault decreases more rapidly than the permeability of the basement. After four months, faults and basement have permeabilities of approximately 1.1×10^{-14} m^2 (Figure 15). After approximately three years, the permeability of the fault is 2.0×10^{-15} m^2, which is close to the preseismic values. The difference between the preseismic and postseismic fault permeabilities can be attributed to external factors that will be discussed in the next section.

[34] If the basal fluid flux were to decrease, for example due to reduced magmatic activity in the TFZ, and permeability enhancement does not occur, the TFZ can preserve elevated pore pressures for approximately less than four months (Figure 16). Figure 16 shows the decay of the pore pressures as a function of time in the fault and basement when the high basal fluid flux is reduced. During the first four months the decrease in pore pressure is much faster than during the following years. Pore pressures have returned to background values after 10 years. Note the vastly different scales of ~700 years for the pore pressure buildup and ~10 years for the pore pressure decay.

5. Discussion

[35] Our simulations present new insights into the preseismic, coseismic and postseismic fluid flow, pore pressure, and permeability evolution in the TFZ. They indicate that the TFZ is characterized by a critically pressured deep crust where the faults have pore pressures close to lithostatic pressure.

[36] Since the exact permeability distribution and basal fluid fluxes, i.e. mantle- and magma-degassing rates, for the TFZ are unknown, a large number of permeability–fluid flux combinations could cause similar pore pressure distributions in the TFZ. While a detailed parametric analysis is beyond the scope of this study and we only want to analyze the principal mechanisms occurring during seismicity-induced fluid flow using a geologically reasonable model and parameter distribution, some further insight can be gained by rewriting the pressure diffusion equation (equation (3)) as

$$\frac{\partial P_f^*}{\partial t} = \eta \nabla^2 P_f^* + \Gamma, \tag{8}$$

where η is the hydraulic diffusivity defined as $\eta = k/\mu_f \beta_f$ and Γ is the source term. Note that P_f^* indicates that we only consider a reduced driving pressure, i.e. we exclude the hydrostatic fluid pressure component such that the equation expresses only the rate at which the driving fluid pressure propagates through the crust. Since μ_f and β_f depend only weakly on pressure and we assume that temperature and salinity do not change with time, the permeability k and the mantle degassing rate Γ (or Q in equation (3)) have the biggest impact on the rate at which fluid pressure increases and its subsequent distribution. Assuming a constant permeability, which is the case in the first part of our simulations, the characteristic distance of the pressure front is proportional to $2\sqrt{\eta t}$. Hence the time at which a steady state pore pressure is reached is the same for different basal fluid fluxes and constant permeabilities, i.e. constant η (Figure 8). However, for a constant fluid flux and varying η, lower permeabilities lead to a faster and more local increase in pore pressure while higher permeabilities have the opposite effect. Hence certain combinations of low permeability and low fluid flux or high permeabilities and high fluid flux should provide

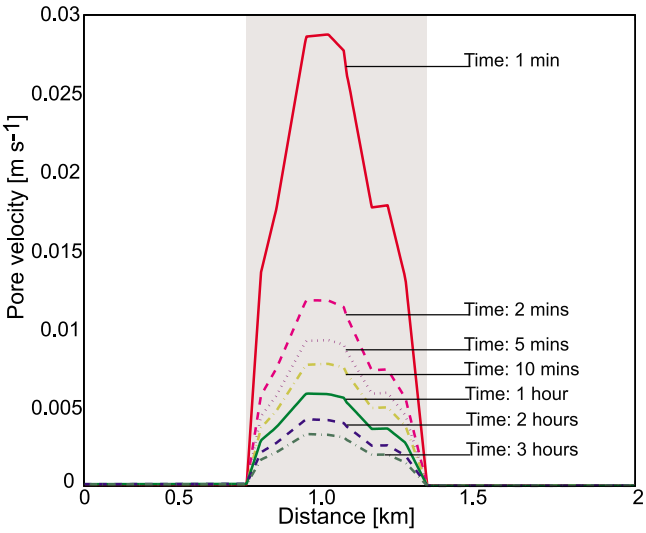

Figure 14. Coseismic and postseismic pore velocity decrease in the fault depicted in Figure 12a at 9 km depth. The jagged lines are artifacts due to interpolating across the unstructured finite element grid. The gray shaded area shows the velocity variation within the fault zone.

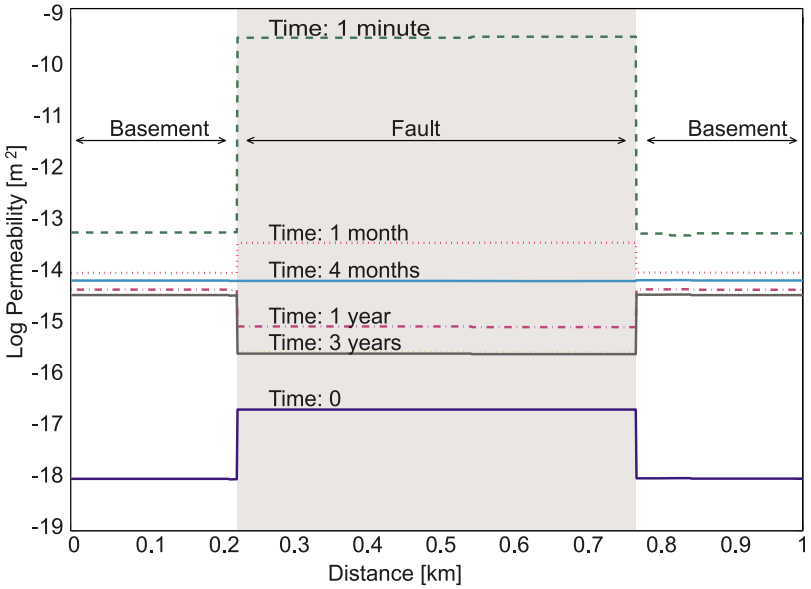

Figure 15. Permeability evolution in the fault and basement depicted in Figure 12a at 9 km depth. The straight lines are due to a limited number of finite elements across the fault. The gray shaded area shows the permeability variation within the fault zone.

pore pressure distributions similar to the ones presented here (Figure 10) but at different timescales. For example, using $k_0 = 10^{-16}$ m^2 in equation (4) for the basement and a fluid flux of 2.0×10^{-9} m s^{-1} also causes elevated pore pressures in the basement and faults; pore pressures are similar to what we have modeled before (Figure 17), but it takes 5.5 kyrs for the pore pressures to build up. While the pore pressure distribution at 9.5 km depth is similar in Figures 10 and 17, the pore pressure distribution in the shallow regions differs strongly. The four regions characterized by elevated pore pressures described above are no longer present and the crust is characterized by elevated pore pressures only at depth. Low pore pressures occur in the TFZ where λ varies from 0.15 to 0.3 between 7.5 km depth and the seafloor.

[38] Since the permeability distribution in the TFZ is not well constrained and there are no direct mantle- and magma-degassing measurements for the TFZ, both pore pressure distributions are equally possible. However, geophysical observations in the TFZ help us to judge which scenario is more likely. In the TFZ most of the shallow and deep fluid-induced seismic events are separated by an aseismic region at intermediate depth. The vertical extent of this area is at least 3 km but could be as large as 10 km [*Hensch et al.*, 2007]. Figure 10, but not Figure 17, shows a region between 4 and 8 km depth with little overpressure, i.e. between the top of the basement and 7.5 km depth. We hence prefer a model with a slightly higher basal fluid flux of 5.4×10^{-9} m s^{-1}, representing the mantle degassing rate, and a permeability decay of $\log_{10}(k) = -14 - 3.2 \log_{10}(z)$ (see equation (4)) in the deeper basement. The resulting pore pressure distribution can best explain the presence of the aseismic region discovered by *Hensch et al.* [2007].

[39] There is some uncertainty in our results as the extensional regime of the TFZ has changed partly to a transtensional regime and vice versa during geological history [*Saemundsson*, 1974; *Garcia et al.*, 2002]. Our 2D simulations also do not account for the complex stress field in 3D faults. Hence we carried out additional simulations for a strike-slip setting but did not observe a significant difference. This is probably because the difference in permeability at a given pore pressure (equations (5) and (6)) does not vary greatly, that is usually less than 20 %, as σ_n approaches zero in an extensional and strike-slip regime. We suspect that a change in permeability of at least an order-of-magnitude is required as σ_n approaches zero to observe a significant change in the flow system.

[40] A pertinent feature emerging from our simulations is that deeper faults have comparatively high pore pressures causing λ to vary between 0.6 and 1 because they focus fluid flow at depth. Upwards fluid migration in the faults of

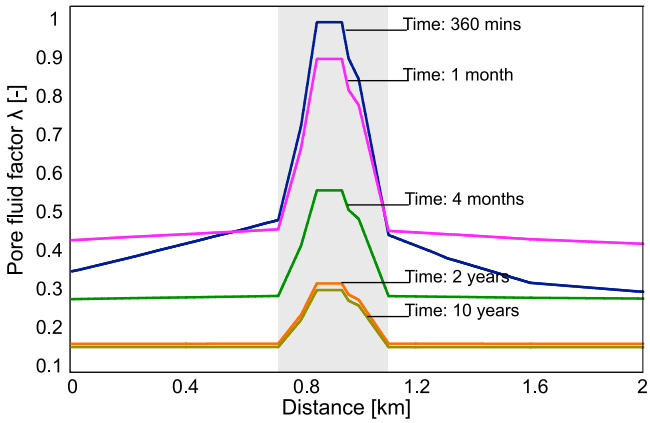

Figure 16. Postseismic reduction in pore fluid factor λ in the basement and fault depicted in Figure 12f at 6.1 km depth. The jagged lines are artifacts due to interpolating across the unstructured finite element grid. The permeability of the faults decreases more rapidly than the permeability of the basement due to different $\hat{k}_0$ and σ^* values. The gray shaded area shows the variation of λ within the fault zone.

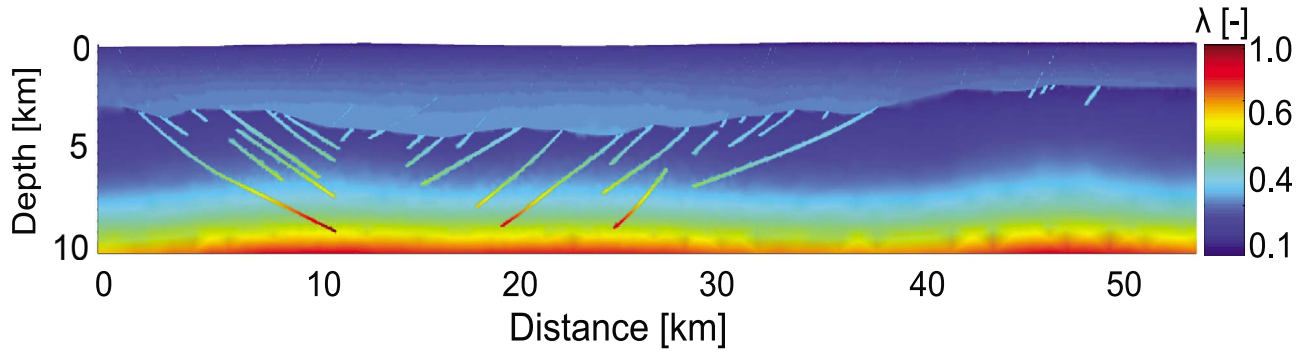

Figure 17. Pore fluid factor λ distribution for a low permeability basement characterized by a permeability that vary as given in equation (4), with $k_0 = 10^{-16}$ m^2 and a low basal fluid flux of 2.0×10^{-10} m s^{-1}. Note that the four distinct regions where elevated pore pressures and high λ values prevail (see Figure 10) are no longer present.

the TFZ is thought to lead to intense microseismicity [*Riedel et al.*, 2001; *Stefánsson et al.*, 2008]. Our simulations offer an explanation for this phenomenon (Figure 12): when faults inflate, pulses of overpressured fluids move upwards in the fault enhancing its permeability. While our model does not reproduce the continuous microseismicity that occurs in the Grimsey Lineament and in the Húsavik Flatey Fault due to the orientation of the seismic profile, it still demonstrates how faults in the TFZ can focus pore pressures (Figure 10) and how pore pressures can diffuse from the faults into the basement, thereby creating small seismic events (Figures 12e–12f).

[41] An important prerequisite to maintain elevated pore pressures in the TFZ is that volatiles degas from the mantle and that the basement and faults have relatively low permeabilities. This is not unreasonable considering (i) that the Icelandic mantle is water-rich and mantle- as well as magma-derived volatiles are present in the TFZ [*Nichols et al.*, 2002; *MacPherson et al.*, 2005] and (ii) that crustal permeabilities are generally decaying as a function of depth [*Manning and Ingebritsen*, 1999; *Saar and Manga*, 2004; *Jiang et al.*, 2010]. If mantle degassing were to stop at all in the TFZ, pore pressures would dissipate in less than 10 years and it may take hundreds of years to build up sufficient pore pressures again. Yet, seismicity-induced fluid flow occurs on much shorter timescales in the TFZ [*Claesson et al.*, 2007]. We hence suggest that regional and moderate mantle degassing rates of approximately 3.0×10^{-9} m s^{-1}, consistent with observed surface degassing rates in South Iceland [*Fridriksson et al.*, 2006] and geochemical analyses in the TFZ [*Nichols et al.*, 2002; *MacPherson et al.*, 2005], maintain elevated pore pressures throughout the TFZ and keep the crust weak. Local changes in mantle degassing rate, for example due to additional dike intrusions [*Hensch et al.*, 2007], can cause the pore pressure to increase locally, leading to fault inflation or dilatant slip. However, certainly not all seismicity in the TFZ can be attributed to elevated pore pressures: Large-scale tectonics that repeatedly cause high-magnitude events in the TFZ and release stress locally are well documented in the TFZ [*Garcia et al.*, 2002; *Stefánsson et al.*, 2008].

[42] An important observation in our simulations is that permeability increase and decay occur over very short timescales, that is between minutes and a few years. This is in agreement with the concept that fault-controlled permeability of seismically active hydrothermal tectonic setting, like the TFZ, is regenerated rapidly due to the presence of fluid flow [*Cox*, 2010]. It is noteworthy that these short timescales are in contrast to low-temperature regions with active seismicity and faulting. In these settings, permeability recovery appears to occur over much longer timescales, i.e. decades [*Crutchley et al.*, 2010; *Rowland et al.*, 2008; *Rowland and Manga*, 2009]. The different timescales in permeability recovery in low- and high-temperature systems may be due to the fact that thermomechanical stresses and mineral precipitation occur at fast rates and are hence able to alter fault permeabilities rapidly in hot hydrothermal system [*Lowell et al.*, 1993]. *Claesson et al.* [2007] have suggested that faults may seal within two years based on their monitoring of the hydrogeochemistry at Húsavik during a seismic cycle. Our simulations show that the cycle of coseismic permeability increase and postseismic permeability decay can be completed in approximately this time frame. The decrease in effective fault normal stress, due to a dissipation of pore pressures, is sufficient to reduce the fault permeability close to the original (low) values. However, as long as an increased mantle degassing rate is present, fault permeabilities will remain elevated to accommodate the extra flow and prevent significant pore pressure buildup. Although mineral precipitation is thought to occur at a slower rate than thermomechanical stresses it is probably critical to seal faults [*Lowell et al.*, 1993] and needed to complete the toggle switch cycle; only if the fault permeability has decreases sufficiently, pore pressure buildup can reoccur within a few years.

[43] The permeability enhancement of faults is also thought to play an important role during the postseismic mixing of shallow and deep fluids [*Claesson et al.*, 2004]. While our model explains the observed postseismic mixing which leads to distinct changes in hydrogeochemistry [*Claesson et al.*, 2004] by rapid upward migration of fluids within faults and possibly from fault to fault at rates of up to 0.03 m s^{-1}, it cannot readily explain the observed hydrogeochemical variations immediately before a seismic event. However, faults are characterized in the preseismic state by higher pore pressures than the surrounding rocks (Figure 10). In this situation, hydrofracture dilatancy can reopen and align fractures in the damaged areas of the faults [*Sibson*, 1981]. This can allow shallow and deep fluids to mix during the preseismic

state although at significantly slower rates compared to immediate coseismic mixing.

[44] For the assumed basement and fault porosities of 2%, our simulated pore velocities of 0.03 m s^{-1} explain the coseismic velocities observed by *Hensch et al.* [2007] for the TFZ. Similar fluid velocities have also been modeled by *Miller et al.* [2004] for the 1997 seismic sequence in Italy, which was caused by the escape of deep fluids from an overpressured reservoir but occurred in a different tectonic setting. Geological evidence [*Okamoto and Tsuchiya*, 2009] further suggests that such short-lived extreme velocity events may be the rule rather than the exception in hydrothermal systems. This includes continental hydrothermal systems as well. For example, *Cathles and Shannon* [2007] have shown that large hydrothermal ore deposits may be formed in tens to hundred of years due to short-lived extreme flow events and local permeability enhancement due to elevated pore pressures may be the key to form economically viable deposits in hydrothermal systems [*Cox and Ruming*, 2004].

6. Conclusions

[45] We simulated the preseismic, coseismic and postseismic fluid flow and the coseismic and postseismic fault permeability behavior using a representative P-T-X distribution in the geologically complex crust of the Tjörnes Fracture Zone (TFZ). Our simulations resolve geological processes acting across vastly different timescales, ranging from minutes to a few years. From this we can draw the following conclusions:

[46] The distribution of pore pressures and their maximum values in the TFZ vary as a function of the mantle degassing rates and crustal permeability. The time required to reach a steady state pore pressure distribution in the TFZ is most likely a few hundred years, assuming a moderate mantle degassing rate of 3.0×10^{-9} m s^{-1} and reasonable permeability distributions. Afterwards, four clearly defined horizontal regions characterized by elevated pore pressures occur in the TFZ. The shallow crust is characterized by low pore pressures, resulting in low pore fluid factors, λ, of approximately 0.15 while in the sedimentary basins λ varies between 0.15 and 0.5. Low pore pressures with λ close to 0.15 occur in the area below the top of the basement. Values of $\lambda \approx 0.6$ are reached around 7.5 km depth. The deep basement is characterized by elevated pore pressures, i.e. well above hydrostatic pressure, and λ between 0.6 and 1.The faults always comprise higher pore pressures than the surrounding structures. At depth they are characterized by critical pore pressures, i.e. they are close to lithostatic pressure (λ approximately 1), which could explain the intense microseismicity observed in the Grimsey Lineament and in the Húsavik Flatey Fault as well as the elevated pore pressures that are thought to prevail in the Húsavik Flatey Fault.

[47] Elevated pore pressures, possibly close to lithostatic pressures, are released by fault inflation. This is probably connected to seismic events. Pore pressures migrate upwards along the fault planes, allowing for deep and shallow fluids to mix. During this phase, pore velocities can exceed 0.01 m s^{-1} and transport chemically different fluids over long distances in short time, as observed in the TFZ. Pore pressure migration in the faults during fault inflation is accompanied by a large increase in permeability of up to 7 orders in magnitude as the effective fault normal stress decreases. While the pore pressure propagation and permeability increase occur within few minutes, timescales for postseismic fault sealing range from 2 to 3 years.

[48] Our simulations show that a toggle switch mechanism is consistent with a number of geophysical and geochemical observations in the Tjörnes Fracture Zone and could explain the inferred links between seismicity and fluid movement in this tectonically and hydrothermally active oceanic setting. A complete toggle switch cycle in the TFZ probably occurs within a few years and is accompanied by very short-lived and extreme fluid fluxes. Repeated cycles continually regenerate fault-controlled permeability and weaken the crust. However, a moderate mantle degassing rate is needed to maintain elevated pore pressures over time. This is not unreasonable because the Icelandic mantle is water-rich and mantle-derived as well as magma-derived volatiles are present in the Tjörnes Fracture Zone.

[49] On a more general note, the recent advances in simulating coupled fluid flow processes in hydrothermal systems now allow for high-resolution models where key geological structures can be represented at great detail [*Ingebritsen et al.*, 2010]. High-resolution simulations like the ones presented here now provide additional means to interpret geophysical data, such as the time series of 16,000 seismic events recorded at the 2003–2004 Ubaye seismic swarm in France [*Daniel et al.*, 2011], and link these data quantitatively with the evolution of fluid flow, pore pressure, effective stress, and fault permeability.

[50] **Acknowledgments.** We thank the Edinburgh Collaborative of Subsurface Science and Engineering, a joint research institute of the Edinburgh Research Partnership in Engineering and Mathematics, for supporting this work. We also thank Susan Agar, Lillemor Claesson, Helen Lewis, John Cosgrove, Alasdair Skelton, and Agust Gudmundsson for fruitful discussions. The help of Bjarni Richter in making data available to us is greatly appreciated. The manuscript benefitted greatly from the careful reviews of three anonymous reviewers and the Associate Editor.

References

Allen, R. M., et al. (2002), Plume-driven plumbing and crustal formation in Iceland, *J. Geophys. Res.*, *107*(B8), 2163, doi:10.1029/2001JB000584.

Bergerat, F., and J. Angelier (2007), Immature and mature transform zones near a hot spot: The South Iceland Seismic Zone and the Tjörnes Fracture Zone (Iceland), *Tectonophysics*, *447*(1–4), 35–46.

Bergerat, F., J. Angelier, and C. Homberg (2000), Tectonic analysis of the Húsavik Flatey Fault (northern Iceland) and mechanisms of an oceanic transform zone, the Tjörnes Fracture Zone, *Tectonics*, *19*(6), 1161–1177.

Bjarnason, I.Th. (2008), An Iceland hotspot saga, *Jokull*, *58*, 3–16.

Bodvarsson, R., S. T. Rögnvaldsson, S. S. Jakobsdóttir, R. Slunga, and R. Stefánsson (1996), The SIL data acquisition and monitoring system, *Seismol. Res. Lett.*, *67*, 35–46.

Cathles, L. M., and R. Shannon (2007), How potassium silicate alteration suggests the formation of porphyry ore deposits begins with the nearly explosive but barren expulsion of large volumes of magmatic water, *Earth Planet. Sci. Lett.*, *262*, 92–108.

Christiansen, L. B., S. Hurwitz, M. O. Saar, S. E. Ingebritsen, and P. A. Hsieh (2005), Seasonal seismicity at western United States volcanic centers, *Earth Planet. Sci. Lett.*, *240*, 307–321.

Claesson, L., A. Skelton, C. Graham, C. Dietl, M. Morth, P. Torssander, and I. Kockum (2004), Hydrogeochemical changes before and after a major earthquake, *Geology*, *32*(8), 641–644.

Claesson, L., A. Skelton, C. Graham, and C. M. Morth (2007), The timescale and mechanisms of fault sealing and water-rock interaction after an earthquake, *Geofluids*, *7*(4), 427–440.

Cox, S. F. (1995), Faulting processes at high fluid pressures: An example of fault valve behavior from the Wattle Gully Fault, Victoria, Australia, *J. Geophys. Res.*, *100*(B7), 12,841–12,859.

Cox, S. F. (2010), The application of failure mode diagrams for exploring the roles of fluid pressure and stress states in controlling styles of fracture-controlled permeability enhancement in faults and shear zones, *Geofluids*, *10*(1–2), 217–233, doi:10.1111/j.1468-8123.2010.00281.x.

Cox, S. F., and K. Ruming (2004), The St Ives mesothermal gold system, western Australia—A case of golden aftershocks?, *J. Struct. Geol.*, *26*(6–7), 1109–1125.

Crutchley, G., S. Geiger, I. A. Pecher, A. R. Gorman, S. A. Henrys, and H. Zhu (2010), The potential influence of shallow gas and gas hydrates on sea floor erosion of Rock Garden, an uplifted ridge offshore of New Zealand, *Geo Mar. Lett.*, *30*(2), 283–303.

Daniel, G., et al. (2011), Changes in effective stress during the 2003-2004 Ubaye seismic swarm, France, *J. Geophys. Res.*, *116*, B01309, doi:10.1029/2010JB007551.

Darbyshire, F. A., I. T. Bjarnason, R. S. White, and Ó. G. Flóvenz (1998), Crustal structure above the Iceland mantle plume imaged by the ICEMELT refraction profile, *Geophys. J. Int.*, *135*(3), 1131–1149.

David, C., T. F. Wong, W. Zhu, and J. Zhang (1994), Laboratory measurement of compaction-induced permeability change in porous rocks: Implications for the generation and maintenance of pore pressure excess in the crust, *Pure Appl. Geophys.*, *143*(1), 425–456.

Driesner, T. (2007), The system H_2O - NaCl. Part II. Correlations for molar volume, enthalpy, and isobaric heat capacity from 0 to 1000 °C, 1 to 5000 bar, and 0 to 1 *X*NaCl, *Geochim. Cosmochim. Acta*, *71*(20), 4902–4919.

Driesner, T., and C. A. Heinrich (2007), The system H_2O - NaCl. Part I: Correlation formulae for phase relations in temperature–pressure–composition space from 0 to 1000 °C, 0 to 5000 bar, and 0 to 1 XNaCl, *Geochim. Cosmochim. Acta*, *71*(20), 4880–4901.

Einarsson, P. (1991), Earthquakes and present-day tectonism in Iceland, *Tectonophysics*, *189*(1–4), 261–279.

Evans, J. P., C. B. Forster, and J. V. Goddard (1997), Permeability of fault-related rocks, and implications for hydraulic structure of fault zones, *J. Struct. Geol.*, *19*(11), 1393–1404.

Flóvenz, Ó. G. (2008), On geothermal energy in Iceland, paper presented at 11th International Symposium on District Heating and Cooling, Univ. of Iceland, Reykjavik.

Flóvenz, Ó. G., and K. Saemundsson (1993), Heat flow and geothermal processes in Iceland, *Tectonophysics*, *225*(1–2), 123–138.

Fridriksson, T., B. R. Kristjánsson, H. Ármannsson, E. Margrétardóttir, S. Ólafsdóttir, and G. Chiodini (2006), CO_2 emissions and heat flow through soil, fumaroles, and steam heated mud pools at the Reykjanes geothermal area, SW Iceland, *Appl. Geochem.*, *21*(9), 1551–1569.

Garcia, S., J. Angelier, F. Bergerat, and C. Homberg (2002), Tectonic analysis of an oceanic transform fault zone based on fault-slip data and earthquake focal mechanisms: The Húsavik Flatey Fault zone, Iceland, *Tectonophysics*, *344*(3–4), 157–174.

Geiger, S., T. Driesner, C. A. Heinrich, and S. K. Matthäi (2005), On the dynamics of H_2O - NaCl fluid convection in the Earth's crust, *J. Geophys. Res.*, *110*(B7), B07101, doi:10.1029/2004JB003362.

Geiger, S., T. Driesner, C. A. Heinrich, and S. K. Matthäi (2006), Multiphase thermohaline convection in the Earth' s crust, I. A new finite element–finite volume solution technique combined with a new equation of state for NaCl - H_2O, *Transp. Porous Media*, *63*(3), 399–434.

Gudmundsson, A. (1993), On the structure and formation of fracture zones, *Terra Nova*, *5*(3), 215–224.

Gudmundsson, A. (2007), Infrastructure and evolution of ocean-ridge discontinuities in Iceland, *J. Geodyn.*, *43*(1), 6–29.

Gunnarsson, K. (1998), Sedimentary basins of the N-Iceland shelf, Rep. OS-98014, Orkustofnun, Reykjavik.

Henry, P. (2000), Fluid flow at the toe of the Barbados accretionary wedge constrained by thermal, chemical, and hydrogeologic observations and models, *J. Geophys. Res.*, *105*(B11), 25,855–25,872.

Hensch, M., C. Riedel, J. Reinhardt, and T. Dahm (2007), Hypocenter migration of fluid-induced earthquake swarms in the Tjörnes Fracture Zone (North Iceland), *Tectonophysics*, *447*(1–4), 80–94.

Hill, D. P., F. Pollitz, and C. Newhall (2002), Earthquake-volcano interactions, *Phys. Today*, *55*(11), 41–47.

Husen, S., R. Taylor, R. B. Smith, and H. Healser (2004), Changes in geyser eruption behavior and remotely triggered seismicity in Yellowstone National Park produced by the 2002 m 7.9 Denali fault earthquake, Alaska, *Geology*, *32*(6), 537–540.

Ingebritsen, S. E., and C. E. Manning (2010), Permeability of the continental crust: Dynamic variations inferred from seismicity and metamorphism, *Geofluids*, *10*(1–2), 193–205, doi:10.1111/j.1468-8123.2010.00278.x.

Ingebritsen, S. E., W. E. Sanford, and C. Neuzil (2006), Groundwater in Geologic Processes, Cambridge Univ. Press, New York.

Ingebritsen, S. E., S. Geiger, S. Hurwitz, and T. Driesner (2010), Numerical simultion of magmatic hydrothermal systems, *Rev. Geophys.*, *48*, RG1002, doi:10.1029/2009RG000287.

Jaeger, J. C., N. G. W. Cook, and R. W. Zimmerman (2007), Fundamentals of Rock Mechanics, Blackwell, Malden, Mass.

Jakobsdóttir, S. (2008), Seismicity in Iceland: 1994–2007, *Jökull*, *58*, 75–100.

Jiang, X. W., X. S. Wan, and L. Wan (2010), Semi-empirical equations for the systematic decrease in permeability with depth in porous and fractured media, *Hydrogeol. J.*, *18*, 839–850, doi:10.1007/s10040-010-0575-3.

Johnson, H. P., M. Hutnak, R. P. Dziak, C. G. Fox, I. Urcuyo, J. P. Cowen, J. Nabelek, and C. Fisher (2000), Earthquake-induced changes in a hydrothermal system on the Juan de Fuca mid ocean ridge, *Nature*, *407*, 174–177.

Lowell, R. P., P. Van Capellen, and L. N. Germanovich (1993), Silica precipitation in fractures and the evolution of permeability in hydrothermal upflow zones, *Science*, *260*(5105), 192–194.

Lupi, M., S. Geiger, and C. Graham (2010), Hydrothermal fluid flow within a tectonically active rift–ridge transform junction: The Tjörnes Fracture Zone, Iceland, *J. Geophys. Res.*, *115*, B05104, doi:10.1029/2009JB006640.

MacPherson, C. G., D. R. Hilton, D. F. Mertz, and T. J. Dunai (2005), Sources, degassing, and contamination of CO_2, H_2O, He, Ne, and Ar in basaltic glasses from Kolbeinsey Ridge, North Atlantic, *Geochim. Cosmochim. Acta*, *69*(24), 5729–5746.

Manga, M., and E. Brodsky (2006), Seismic triggering of eruptions in the far field: Volcanoes and geysers, *Annu. Rev. Earth Planet. Sci.*, *34*, 263–291.

Manning, C. E., and S. E. Ingebritsen (1999), Permeability of the continental crust: Implications of geothermal data and metamorphic systems, *Rev. Geophys.*, *37*(1), 127–150.

Miller, S. A., and A. Nur (2000), Permeability as a toggle switch in fluid-controlled crustal processes, *Earth Planet. Sci. Lett.*, *183*, 133–146.

Miller, S. A., C. Collettini, L. Chiaraluce, M. Cocco, M. Barchi, and B. J. P. Kaus (2004), Aftershocks driven by a high-pressure CO_2 source at depth, *Nature*, *427*, 724–727.

Nichols, A. R. L., M. R. Carroll, and A. Höskuldsson (2002), Is the Iceland hot spot also wet? Evidence from the water contents of undegassed submarine and subglacial pillow basalts, *Earth Planet. Sci. Lett.*, *202*, 77–87.

Okamoto, A., and N. Tsuchiya (2009), Velocity of vertical fluid ascent within vein-forming fractures, *Geology*, *37*(6), 563–566.

Paluszny, A., S. K. Matthai, and M. Hohmeyer (2007), Hybrid finite element-finite volume discretization of complex geologic structures and a new simulation workflow demonstrated on fractured rocks, *Geofluids*, *7*(2), 186–208.

Peng, S., and J. Zhang (2007), *Engineering Geology for Underground Rocks*, Springer, New York.

Revil, A., and L. M. Cathles (2002), Fluid transport by solitary waves along growing faults: A field example from the South Egene Island Basin, Guld of Mexico, *Earth Planet. Sci. Lett.*, *202*, 321–335.

Rice, J. R. (1992), Fault stress states, pore pressure distributions, and the weakness of the San Andreas Fault, in *Fault Mechanics and Transport Properties of Rocks*, *Int. Geophys. Series*, vol. 51, edited by B. Evans and T.-f. Wong, pp. 475–475, Academic, New York.

Richter, B. (2006), Structure of the Törnes basin, north Iceland; possible forming of oil and gas within a young, shallow sedimentary basin with high geothermal gradient, Internal report, Orkustofnun, Reykjavik.

Riedel, C., M. Schmidt, R. Botz, and R. Theilen (2001), The Grimsey hydrothermal field offshore North Iceland: Crustal structure, faulting and related gas venting, *Earth Planet. Sci. Lett.*, *193*, 409–421.

Riedel, C., A. Tryggvason, T. Dahm, R. Stefanson, R. Bödvarson, and G. B. Gudmundsson (2005), The seismic velocity structure north of Iceland from joint inversion of local earthquake data, *J. Seismol.*, *9*(4), 383–404.

Roeloffs, E., M. Sneed, D. L. Galloway, M. L. Sorey, C. D. Farrar, J. F. Howle, and J. Hughes (2003), Water-level changes induced by local and distant earthquakes at Long Valley Caldera, California, *J. Volcanol. Geotherm. Res.*, *127*(3–4), 269–303.

Rögnvaldasson, S. T., A. Gudmundsson, and R. Slunga (1998), Seismotectonic analysis of the Tjörnes Fracture Zone, an active transform fault in North Iceland, *J. Geophys. Res.*, *103*(B12), 30,117–30,129.

Rojstaczer, S. A., S. E. Ingebritsen, and D. O. Hayba (2008), Permeability of continental crust influenced by internal and external forcing, *Geofluids*, *8*(2), 128–139.

Rowland, J. C., and M. Manga (2009), Response of Alum Rock springs to the October 30, 2007 Alum Rock earthquake and implications for the origin of increased discharge after earthquakes, *Geofluids*, *9*(3), 237–250.

Rowland, J. C., M. Manga, and T. P. Rose (2008), The influence of poorly interconnected fault zone flow paths on spring geochemistry, *Geofluids*, *8*(2), 93–101.

Rubey, W. W., and M. K. Hubbert (1965), Role of fluid pressure in mechanics of overthrust, *Geol. Soc. Am. Bull.*, *76*, 469–474.
Saar, M. O., and M. Manga (2004), Depth dependence of permeability in the oregon cascades inferred from hydrogeologic, thermal, seismic, and magmatic modeling constraints, *J. Geophys. Res.*, *109*, B04204, doi:10.1029/2003JB002855.
Saemundsson, K. (1974), Evolution of the axial rifting zone in Northern Iceland and the Tjörnes Fracture Zone, *Geol. Soc. Am. Bull.*, *85*, 495–504.
Sibson, R. H. (1974), Frictional constraints on thrust, wrench and normal faults, *Nature*, *249*, 542–544.
Sibson, R. H. (1981), Controls on low-stress hydro-fracture dilatancy in thrust, wrench and normal fault terrains, *Nature*, *289*, 665–667.
Sibson, R. H. (1985), Stopping of earthquake ruptures at dilational fault jogs, *Nature*, *316*, 248–251.
Sibson, R. H. (1990), Conditions for fault-valve behaviour, *Geol. Soc. Spec. Publ.*, *54*(1), 15–28.
Sibson, R. H. (1992), Implications of fault-valve behaviour for rupture nucleation and recurrence, *Tectonophysics*, *211*(1–4), 283–293.
Sibson, R. H. (2007), An episode of fault-valve behaviour during compressional inversion?—The 2004 M 6.8 mid-Niigata prefecture, Japan, earthquake sequence, *Earth Planet. Sci. Lett.*, *257*, 188–199.
Sigmundsson, F. (2006), Iceland Geodynamics: Crustal Deformation and Divergent Plate Tectonics, Springer, New York.
Snow, D. T. (1968), Rock fracture spacings, openings, and porosities, *Proc. Am. Soc. Civ. Eng.*, *94*, 73–19.
Spycher, N., K. Pruess, and J. Ennis-King (2003), CO_2-H_2O mixtures in the geological sequestration of CO_2. I. Assessment and calculation of mutual solubilities from 12 to 100°C and up to 600 bar, *Geochim. Cosmochim. Acta*, *67*, 3015–3031.
Spycher, N., and K. Pruess (2005), CO_2-H_2O mixtures in the geological sequestration of CO_2. II. Partitioning in chloride brines at 12–100°C and up to 600 bar, *Geochim. Cosmochim. Acta*, *69*, 3309–3320.
Stanislavsky, E., and G. Garven (2003), A theoretical model for reverse water-level fluctuations induced by transient permeability in thrust fault zones, *Earth Planet. Sci. Lett.*, *210*, 579–586.
Stefánsson, R., G. B. Gudmundsson, and P. Halldórsson (2003), The South Iceland earthquakes 2000: A challenge for earthquake prediction research, report, Veurstofa Íslands, Reykjavik.
Stefánsson, R., G. B. Gudmundsson, and P. Halldórsson (2008), Tjörnes Fracture Zone: New and old seismic evidences for the link between the North Iceland rift zone and the mid atlantic ridge, *Tectonophysics*, *447*(1–4), 117–126.
Stigall, J., and B. Dugan (2010), Overpressure and earthquake initiated slope failure in the Ursa region, northern Gulf of Mexico, *J. Geophys. Res.*, *115*, B04101, doi:10.1029/2009JB006848.
Terzaghi, K. (1925), *Erdbaumechanik*, Deuticke, Wien, Austria.
Terzaghi, K. (1923), Die Berechnung der Durchlässigkeitsziffer des Tones aus dem Verlauf der Hydrodynamischen Spannungserscheinungen, Anz. Akad. Wiss. Wien, *Math. Naturwiss. Kl.*, *132*, 125–138.
Townend, J., and M. D. Zoback (2000), How faulting keeps the crust strong, *Geology*, *28*(5), 595–598.
Wiprut, D., and M. D. Zoback (2000), Fault reactivation and fluid flow along a previously dormant normal fault in the Northern North Sea, *Geology*, *28*(7), 595–598.
Zoback, M. D., and J. C. Zinke (2002), Production-induced normal faulting, *Pure Appl. Geophys.*, *159*(1–3), 403–420.
Zoback, M. D., C. A. Barton, M. Brudy, D. A. Castillo, T. Finkbeiner, B. R. Grollimund, D. B. Moos, P. Peska, C. D. Ward, and D. J. Wiprut (2003), Determination of stress orientation and magnitude in deep wells, *Int. J. Rock Mech. Min. Sci.*, *40*(7–8), 1049–1076.

S. Geiger, Institute of Petroleum Engineering, Heriot-Watt University, Edinburgh EH14 4AS, UK.
C. M. Graham, School of Geosciences, University of Edinburgh, Grant Institute, The King's Buildings, West Mains Road, Edinburgh EH9 3JW, UK.
M. Lupi, Steinmann Institute, Department of Geodynamics, University of Bonn, Nussalle 8, D-53115 Bonn, Germany. (matteo.lupi@gmail.com)